A&A 594, A58 (2016)
DOI: 10.1051/0004-6361/201628519

Astronomy & Astrophysics

The segregation of starless and protostellar clumps in the Hi-GAL $\ell = 224°$ region⋆

L. Olmi[1,2], M. Cunningham[3], D. Elia[4], and P. Jones[3]

[1] INAF, Osservatorio Astrofisico di Arcetri, Largo E. Fermi 5, 50125 Firenze, Italy
e-mail: olmi.luca@gmail.com
[2] University of Puerto Rico, Rio Piedras Campus, Physics Dept., Box 23343, UPR station, San Juan, Puerto Rico, USA
[3] School of Physics, University of New South Wales, 2052 Sydney, Australia
[4] INAF, Istituto di Astrofisica e Planetologia Spaziali, via Fosso del Cavaliere 100, 00133 Roma, Italy

Received 15 March 2016 / Accepted 16 July 2016

ABSTRACT

Context. Stars form in dense, dusty structures, which are embedded in larger clumps of molecular clouds often showing a clear filamentary structure on large scales (≳1 pc). The origin (e.g., turbulence or gravitational instabilities) and evolution of these filaments, as well as their relation to clump and core formation, are not yet fully understood. A large sample of both starless and protostellar clumps can now be found in the *Herschel* Infrared GALactic Plane Survey (Hi-GAL) key project, which also provides striking images of the filamentary structure of the parent molecular clouds. Recent results indicate that populations of clumps on and off filaments may differ.

Aims. One of the best-studied regions in the Hi-GAL survey can be observed toward the $\ell = 224°$ field. Here, a filamentary region has been studied and it has been found that protostellar clumps are mostly located along the main filament, whereas starless clumps are detected off this filament and are instead found on secondary, less prominent filaments. We want to investigate this segregation effect and how it may affect the clumps properties.

Methods. We mapped the ^{12}CO (1−0) line and its main three isotopologues toward the two most prominent filaments observed toward the $\ell = 224°$ field using the Mopra radio telescope, in order to set observational constraints on the dynamics of these structures and the associated starless and protostellar clumps.

Results. Compared to the starless clumps, the protostellar clumps are more luminous, more turbulent and lie in regions where the filamentary ambient gas shows larger linewidths. We see evidence of gas flowing along the main filament, but we do not find any signs of accretion flow from the filament onto the Hi-GAL clumps. We analyze the radial column density profile of the filaments and their gravitational stability.

Conclusions. The more massive and highly fragmented main filament appears to be thermally supercritical and gravitationally bound, assuming that all of the non-thermal motion is contributing thermal-like support, suggesting a later stage of evolution compared to the secondary filament. The status and evolutionary phase of the Hi-GAL clumps would then appear to correlate with that of the host filament.

Key words. stars: formation – ISM: clouds – ISM: molecules

1. Introduction

Stars form in dense, dusty structures, which are embedded in larger clumps of molecular clouds. Here, the term clump refers to any compact density enhancement (with size ∼0.1−1 pc and density $\sim 10^4$−10^5 cm^{-3}), as identified by source-extraction algorithms, and core (size ≲0.01−0.1 pc and density ≳10^5 cm^{-3}) refers to the clump sub-structures which are going to form stars. A large sample of both starless (i.e., with no sign of active star formation, and not necessarily gravitationally bound) and protostellar clumps can now be found in the *Herschel* Infrared GALactic Plane Survey (Hi-GAL) key project (Molinari et al. 2010). The Hi-GAL survey also provides striking images of the filamentary structure of the parent molecular clouds on large scales (≳1 pc), which now allow to study the physical connection between the clumps/cores and the filaments. Filamentary structures were known to be present in molecular clouds even before the recent large scale star-formation surveys at far-infrared wavelengths. The origin (e.g., turbulence or gravitational instabilities) and evolution of these filaments, as well as their relation to star formation, are not yet fully understood.

Observationally, filaments show complex structures with multiple branches and hubs, where the dense clumps/cores detected in the Hi-GAL survey are more frequently found. The observed similarity between the mass distribution of the clumps and the stellar initial mass function (IMF) supports the accepted idea that clumps may fragment into sub-structures (cores or fragments) which then form stars or even clusters of stars. Therefore, in order to draw a more complete picture of star formation it is fundamental to study the transition phase from the observed clump mass function (CMF) to the IMF, and to understand how the presence of filaments affects the formation of clumps and their mass distribution.

Two interesting recent results have been published as part of the *Herschel* Gould Belt Survey (HGBS, André et al. 2010). Polychroni et al. (2013) studied the L 1641 molecular clouds in Orion A and found that most (≃70%) of the starless clumps

⋆ Mopra data are only available at the CDS via anonymous ftp to cdsarc.u-strasbg.fr (130.79.128.5) or via http://cdsarc.u-strasbg.fr/viz-bin/qcat?J/A+A/594/A58

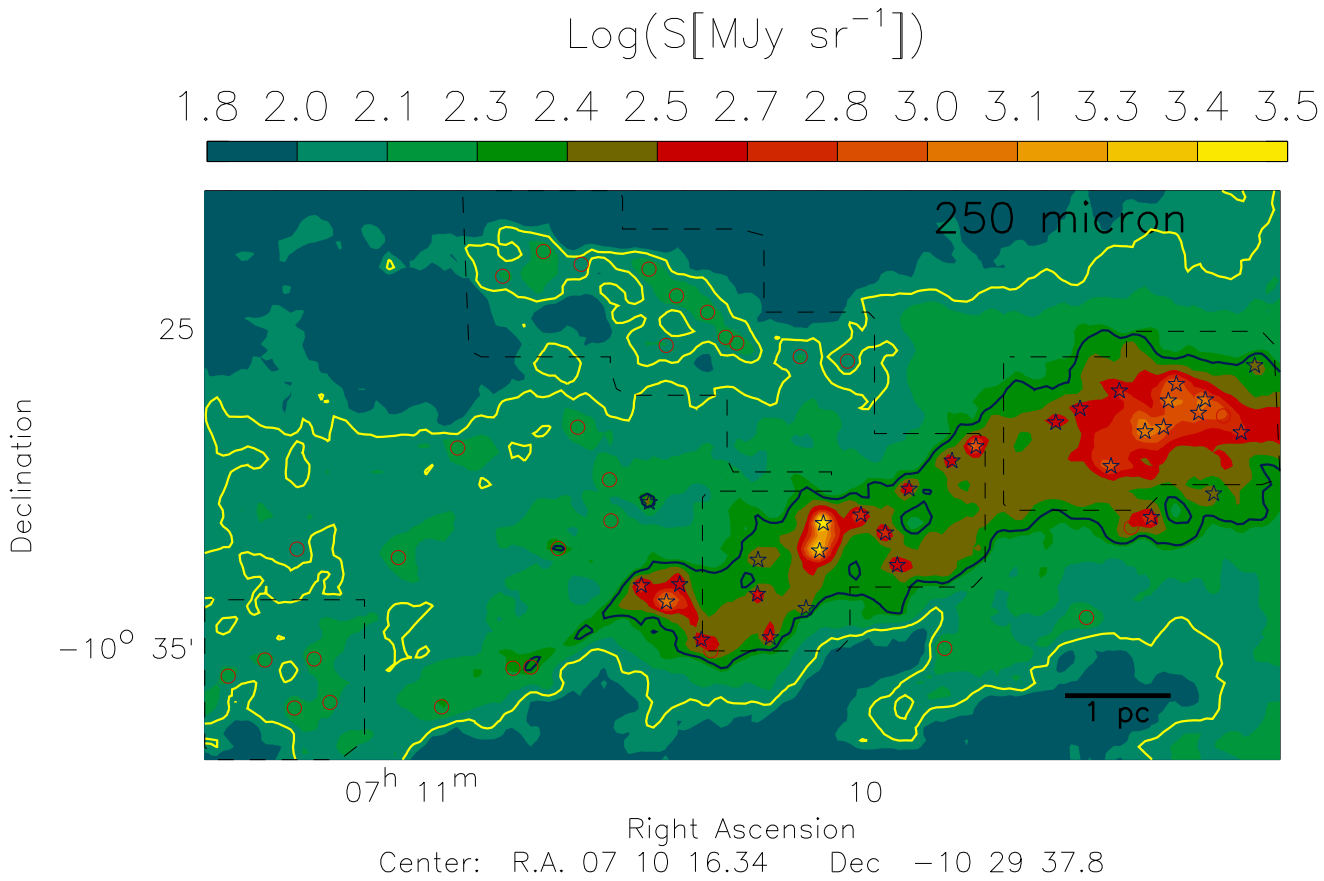

Fig. 1. SPIRE 250 μm emission observed toward the $\ell = 224°$ region, with a (logarithmic) color-scale in MJy sr^{-1} (Elia et al. 2013). Blue star symbols represent protostellar clumps while the red empty circles represent starless clumps. The dashed, black contour shows the region mapped with the Mopra telescope. The yellow and blue solid contours correspond to about 100 and 200 MJy sr^{-1}, respectively, and approximately trace the secondary filament toward the north (besides to low-level emission from the main filament) and the main filament.

were located on filaments. They also found that the two clump populations (on and off the identified filaments) had distinctly different CMF. In a separate work, Arzoumanian et al. (2013) investigated the gas velocity dispersions of a sample of filaments, also detected as part of the HGBS in the IC 5146, Aquila, and Polaris interstellar clouds. They found that these filaments could be divided into two regimes: (i) thermally subcritical filaments, gravitationally unbound; and (ii) thermally supercritical filaments, which have higher velocity dispersions and are self-gravitating. These authors propose that, as they contract and accrete material from the background cloud, supercritical filaments are expected to fragment into clumps and form (proto)stars (as supported by some theoretical models, e.g., Pon et al. 2011). On the other hand, Schneider et al. (2010) analyzed the dynamics of the DR21 high-mass star-forming region and found that its filamentary morphology, and the existence of sub-filaments, can be explained if the DR21 filament was formed by the convergence of gas flows on large scales.

In their works, Polychroni et al. (2013) completely ignore the protostellar clumps, while Arzoumanian et al. (2013) and Schneider et al. (2010) do not correlate the study of the filament dynamics with the presence of starless and protostellar clumps. In addition, the massive DR21 region is quite different from the molecular clouds studied in the HGBS, and thus the question arises of whether different filament dynamics may lead to different (low- and high-mass) star formation. Molecular line mapping of a larger sample of filaments is thus required, in order to set stronger observational constraints on the dynamics of these structures.

2. Observations

2.1. Hi-GAL observations

The Hi-GAL survey offers the best opportunity to look at large clump populations in various clouds with different physical conditions, while using self-consistent analysis to derive their physical parameters (see, e.g., Elia et al. 2010, 2013; Olmi et al. 2013). Mass and other physical parameters of the Hi-GAL clumps were derived from a single-temperature spectral energy distribution (SED) model applied to suitable candidates in the Hi-GAL catalog. To extract candidate sources, a first catalog based on image photometry was compiled in each of the observed Hi-GAL fields, identifying the sources detected in the five different bands based on simple positional association.

One of the best-studied regions in the Hi-GAL survey is found in the $\ell = 217°-224°$ field. The filamentary structure in this field has been studied by Schisano et al. (2014), while Elia et al. (2013) identified a well-defined and isolated filamentary cloud, at $\ell \simeq 224°$ and a distance of about 1.0 kpc, with clear signs of star formation (see Fig. 1). The most peculiar property of this cloud is the segregation observed between starless and protostellar clumps. In fact, protostellar clumps are mostly found along the main filament (filament here is used qualitatively to

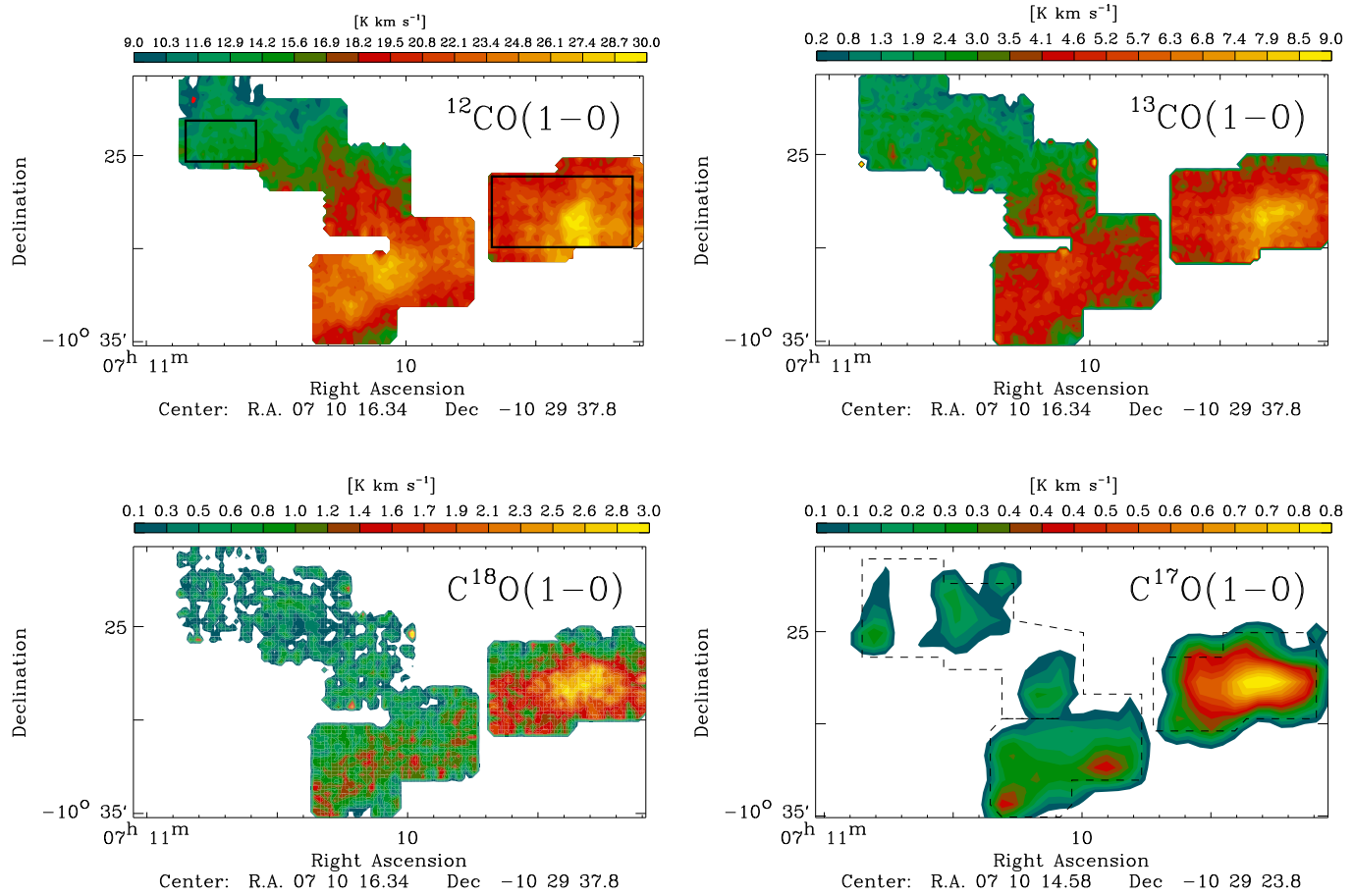

Fig. 2. Maps of the line integrated intensity, $\int T_A^\star \mathrm{d}v$, observed toward the $\ell = 224°$ region in the various CO isotopologues. *From left to right* and *from top to bottom*: ^{12}CO(1−0), ^{13}CO(1−0), C^{18}O(1−0) and C^{17}O(1−0). The map of C^{17}O(1−0) has been convolved to an 80″ beam and regridded to a 40″ spacing to increase the S/N. The black boxes represent two of the regions where spectra have been averaged and shown in Fig. 4.

indicate an elongated or threadlike structure, and we do not use a specific operational definition; see also Sect. 5.1), whereas starless clumps are detected off this filament and are instead found on secondary, less prominent filaments (see Fig. 1). Therefore, also in this region most clumps are indeed located on filaments, as already noted by Polychroni et al. (2013), but the segregation in terms of clump type observed here has not yet been reported.

2.2. Mopra

Our observations were carried out with the ATNF Mopra 22-m telescope[1] in Australia, in June 2014. We observed the ^{12}CO (1−0) (115.271202 GHz), ^{13}CO (1−0) (110.201353 GHz), C^{18}O (1−0) (109.782173 GHz) and C^{17}O (1−0) (112.359280 GHz) spectral lines. The ^{12}CO (1−0) line is known to be optically thick, and thus the other three isotopologues were also observed to provide optical depth and line profile information. Unfortunately, except for ^{13}CO(1−0), their intensity was in general too weak to allow derivation of column densities throughout the map and other useful physical and kinematical parameters, and thus most of our analysis will be based on ^{13}CO(1−0) and partly on C^{18}O(1−0) (from now on the (1−0) will be omitted for simplicity when referring to any of the observed transitions).

[1] The Mopra radio telescope is part of the Australia Telescope National Facility (ATNF) which is funded by the Commonwealth of Australia for operation as a National Facility managed by CSIRO.

We used the single pixel broadband spectrometer, MOPS, which allows for multiple spectral windows to be observed simultaneously. Specifically, MOPS was used in its zoom mode, which allowed to split the 8.3 GHz instantaneous band in up to 16 zoom bands to focus on different molecules of interest. Each sub-band in zoom mode was 137.5 MHz wide and had 2 × 4096 channels, and the spectral resolution was ≃0.09 km s^{-1} for the 90 GHz receiver. During our observations the system temperature was typically comprised in the range ≃240−450 K (^{13}CO and C^{18}O), ≃280−500 K (C^{17}O) and ≃520−920 K (^{12}CO). We reached a RMS sensitivity in $T_A^\star$ units of about ∼0.12−0.18 K (^{13}CO, C^{18}O and C^{17}O) and ∼0.25−0.40 K (^{12}CO) after rebinning to a 0.20 km s^{-1} velocity resolution. The beam full width at half maximum (FWHM) was about 38 arcsec and the pointing was checked every hour by using a SiO maser as a reference source (Indermuehle et al. 2013). Typically, pointing errors were found to be ∼5−10 arcsec. The parameter η_{mb} to convert from antenna temperature to main-beam brightness temperature has been assumed to be 0.44 at 100 GHz and 0.49 at 86 GHz (Ladd et al. 2005).

The single-point observations were performed in position-switching mode, whereas the spectral line maps, composed of individual tiles of size mostly 5 × 5 arcmin^2, were obtained using the Mopra on-the-fly mapping mode, scanning in both right ascension and declination. A total of 8 tiles were observed (see Figs. 1 and 2): seven tiles are mostly contiguous, while an additional tile was observed off the main and secondary filaments and

covers an isolated group of Hi-GAL clumps. The data were reduced with LIVEDATA and GRIDZILLA for the bandpass correction and gridding[2]. The fits cubes were taken into MIRIAD[3] for a 3-pt hanning smoothing and an additional first-order correction to the baselines. The data were then analyzed with the `xs`[4] package of the Onsala Space Observatory, and they were also imported into CLASS[5] and IDL[6] for line parameter measurement and further analysis.

3. Results

3.1. Physical properties of the Hi-GAL clumps

Before analysing the results of the spectral line observations we first show in Fig. 3 a plot of the bolometric luminosities versus the masses of the Hi-GAL clumps (see also Elia et al. 2013). In this plot starless and protostellar sources are represented by the red empty circles and blue star signs, respectively, and one can note immediately that they populate quite different regions of the diagram. The regions occupied by the starless and protostellar sources can be characterized by using the evolutionary tracks discussed by Molinari et al. (2008), who proposed an evolutionary sequence for protostars in terms of two parameters: the envelope mass and the bolometric luminosity. These authors suggest an evolutionary sequence which is concentrated in two main phases: protostars first accrete mass from their envelopes, and later disperse their envelopes by winds and/or radiation. In Fig. 3 the calculated evolutionary tracks thus rise upward in luminosity (almost vertically in the case of high-mass protostars) during the accretion phase, and then proceed horizontally to the left (to lower masses) during the envelope dispersal phase.

As already noted by Elia et al. (2013) protostellar and starless sources populate quite different regions of the diagram, corresponding to the accreting core phase in the first case, and to a quiescent or collapsing core in the second, respectively. In fact, the protostellar sources occupy regions of the diagram at higher temperature, as shown by the loci at constant temperature of a modified blackbody (dashed lines). Although this plot cannot be used to obtain a classical single-YSO classification (see Elia et al. 2013 for a discussion of this point), it suggests as expected an additional type of evolutionary segregation between starless and protostellar clumps, besides to the observed positional segregation discussed in Sect. 2.1.

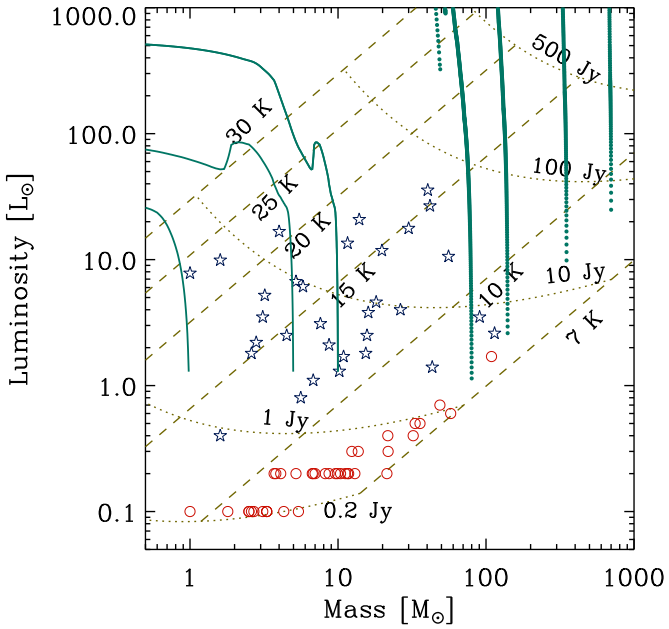

Fig. 3. Clump bolometric luminosity vs. mass, as derived from the Hi-GAL observations. Symbols for starless and protostellar sources are as in Fig. 1. The dotted lines represent loci of constant 250 μm flux density, ranging from 0.1 to 500 Jy, assuming a modified blackbody spectral energy distribution with $\beta = 1.5$ and a fixed distance of ~1 kpc. Roughly orthogonal to these are loci (dashed lines) at constant temperature, for the same modified blackbody. The green solid lines and small green filled circles represent the evolutionary tracks for the low- and high-mass regimes, respectively, taken from Molinari et al. (2008).

3.2. Basic cloud structure: integrated intensity

We present maps of the integrated intensity of the CO isotopologues in Fig. 2. These maps were meant to cover most of the emission from the main and secondary filaments shown in Fig. 1. The main filament is visible as a strip of intense emission from the NW to SE. A secondary, less intense filament, can be observed running from the NE toward the center of the map where it meets the main filament. Although our coverage across the $\ell = 224°$ region is not complete, the observed spectral line maps cover most of the warm dust emission from both main and secondary filaments, as shown in Fig. 1. As mentioned in Sect. 2.2 we also mapped a smaller region, visible in the SE corner of the maps and relatively off the main filament, which contains a small group of starless clumps. However, this isolated tile will not be shown on subsequent maps, for the sake of clarity.

Both ^{13}CO and C^{18}O have a good signal-to-noise ratio (S/N) along the main filament. However, the secondary filament is better traced by ^{12}CO and ^{13}CO. One can see that in general the ^{13}CO and C^{18}O emission closely follows the dust continuum emission, whereas the optically thick ^{12}CO shows significant deviations, as expected. The most intense region of extended emission, located along the main filament in the NW of the Hi-GAL map (at approximately RA ~ $07^h09^m19^s$ and Dec ~ $-10°27'$), is clearly visible in the less optically thick ^{13}CO and C^{18}O tracers. However, we note a lack of correspondence between the C^{18}O emission and the dust continuum peaks which are visible near the center of the Hi-GAL map (at RA ~ $07^h10^m05.8^s$ and Dec ~ $-10°31'30''$). C^{18}O and submillimeter dust continuum emission are both tracers of column density, but they have different dependences on temperature. Therefore, temperature variations, more likely to be observed toward dense clumps, may affect the relative distributions of these two column density tracers (see, e.g., Wilson et al. 1986). In addition, this departure between the C^{18}O and dust continuum emission coincides with the location of several dense clumps and thus another alternative (or additional) explanation for the lack of C^{18}O emission is that that this molecule has depleted from the dense gas (see, e.g., Hacar et al. 2013, and references therein).

3.3. Basic velocity structure: channel maps

The area that we mapped with the Mopra telescope has already been covered by the lower angular resolution (2.7 arcmin) survey

[2] http://www.atnf.csiro.au/computing/software/livedata/index.html
[3] http://bima.astro.umd.edu/miriad/
[4] http://www.chalmers.se/rss/oso-en/observations/data-reduction-software
[5] CLASS is part of the GILDAS software package developed by IRAM.
[6] http://www.exelisvis.com/ProductsServices/IDL.aspx

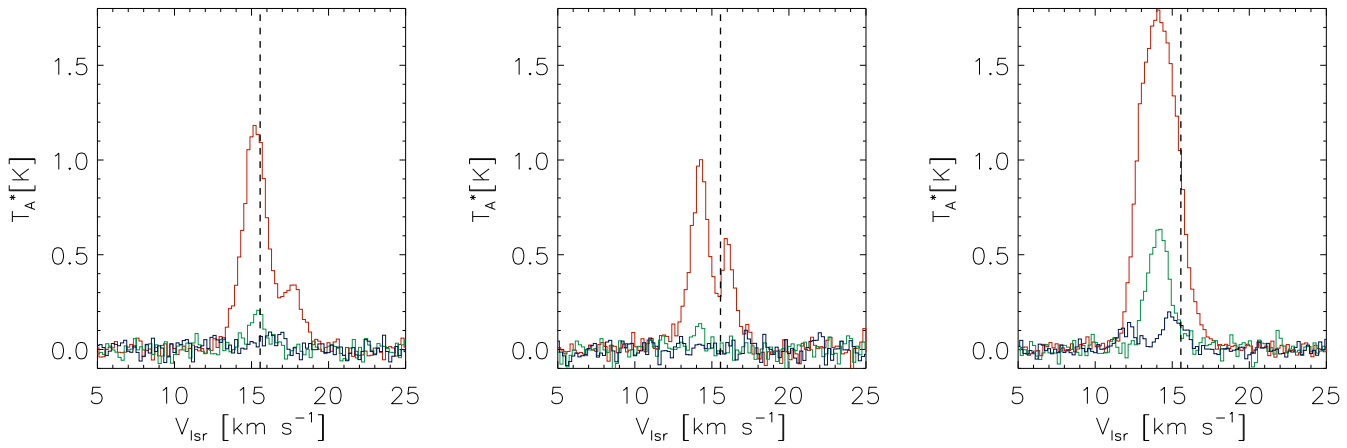

Fig. 4. Positionally averaged spectra of ^{13}CO (red), C^{18}O (green) and C^{17}O(1−0) (blue) lines. The regions considered (*from left to right*) are: a ∼4 × 4 arcmin^2 region around positions (RA ∼ 07^{h}11^{m}18^s, Dec ∼ −10°36′; corresponding to the isolated individual region in the SE); a ∼4 × 2 arcmin^2 region around position (RA ∼ 07^{h}10^{m}42^s, Dec ∼ −10°23′), at the NE end of the secondary filament; and a ∼8 × 3 arcmin^2 region around the bright region of emission toward the NW along the main filament. These last two regions are shown as black boxes in Fig. 2. The dashed vertical line corresponds to the velocity, 15.6 km s^{-1} obtained with a Gaussian fit to the C^{18}O(1−0) line of the first region.

of molecular clouds in the Monoceros and Canis Major regions carried out with the NANTEN telescope in the ^{13}CO (1−0) line (Kim et al. 2004), spanning an area of 560 deg^2. The NANTEN observations were also much less sensitive, with a typical RMS noise of ∼0.5 K. However, although the NANTEN data can be used to estimate the kinematic distances needed to derive masses and luminosities (Elia et al. 2013), higher angular resolution and more sensitive maps are necessary to analyze the column density distribution in the $\ell = 224°$ region.

We show the channel maps of the ^{13}CO and C^{18}O lines in Figs. A.1 and A.2. The distribution of bulk emission in the NW part of the cloud between ∼13.5 and 16 km s^{-1} is similar in both tracers. As mentioned above, the emission toward the center of the field is better detected in the ^{13}CO map. Extended emission from ^{13}CO in both the main and secondary filaments is better viewed at V_{lsr} ∼ 14.2−14.6 km s^{-1}. Emission from the secondary filament appears to be concentrated on a narrower velocity range, compared to emission from the main filament. Along the latter a velocity gradient (see Sect. 4.2.1) is also visible, with emission slowly shifting from the NW (at low velocities) to the SE (at higher velocities). A similar velocity gradient is also observed in the C^{18}O channel map.

The averaged spectra of ^{13}CO, C^{18}O and C^{17}O are shown in Fig. 4. The minor deviations from a Gaussian shape and the relatively large velocity range of emission (≳5 km s^{-1} for ^{13}CO) are a consequence of the velocity gradients in the region. The ^{13}CO emission from two of the regions considered is clearly double-peaked (see also Figs. A.1 and A.3). This appears to be the consequence of two separate cloud components at different velocities (14.4 and 16.2 km s^{-1}), rather than a dip due to self-absorption. In fact, the average C^{18}O(1−0) spectra from the same regions show weak emission to be present at the lower-velocity component, which also appears to be the most intense. However, the limited extent of our maps does not allow us to investigate whether this ^{13}CO double-peaked profile actually corresponds to two entirely different filaments that overlap in projection, as for example observed by Hacar et al. (2013).

An interesting feature is the double-peaked profile of the C^{17}O spectrum toward the main clump of emission. The more intense, high-velocity component corresponds to the same emission as from ^{13}CO and C^{18}O. However, the lower-velocity component, peaking at about 12 km s^{-1}, has no correspondence in the spectra of the more abundant isotopologues, and a clump of emission at this velocity can be clearly seen in Fig. A.5. Given the difference in the typical optical depth of C^{17}O and the other isotopologues, one possibility to explain these data is that the lower-velocity clump is behind the presumably more massive, high-velocity component, thus preventing detection of the less massive clump in the optically thicker ^{13}CO and C^{18}O lines. Figure A.5 also shows another interesting feature, namely, C^{17}O emission along the main filament is clearly detected at different velocities, peaking for example in the 13.6 km s^{-1} channel and then rising again near 16 km s^{-1}. This suggests that these filaments may indeed be characterized by a more complex velocity structure, as observed by Hacar et al. (2013).

4. Analysis

In this section we will discuss the derivation of various physical parameters such as column density, mass and kinetic temperature, that are fundamental for the analysis of the sources. We will also analyse the kinematics of the sources, determining velocity gradients and line asymmetries. The estimate of the virial masses will also allow us to determine which sources are currently gravitationally bound and which are not.

4.1. Opacity, excitation temperature and column density

4.1.1. Results from the ^{13}CO and C^{18}O data

Column densities were derived from the ^{13}CO and C^{18}O data by assuming a filled beam and a uniform excitation temperature (equal for both tracers) within the beam. We follow the standard procedure of deriving the opacity in both lines at each position in the maps, from the ratio, R, of ^{13}CO to C^{18}O main-beam brightness temperatures:

$$R = \frac{T_{\rm mb}[^{13}{\rm CO}]}{T_{\rm mb}[{\rm C}^{18}{\rm O}]} = \frac{1-\exp(-\tau_{13})}{1-\exp(-\tau_{18})}. \quad (1)$$

To reduce the effects of noise, the spectra were binned to a velocity resolution of 0.3 km s^{-1}, and the brightness ratio was only

computed when the S/N was >3 in the $C^{18}O$ data. If we assume an abundance ratio $[^{13}CO]/[C^{18}O] \simeq 7.4$ (Wilson & Rood 1994) then $\tau_{13} \simeq 7\tau_{18}$ and Eq. (1) can thus be solved for τ_{18}. We calculate the opacity of the two CO isotopologues at the peak of the $C^{18}O$ spectrum at each position in the map.

If the optical depth is known, the excitation temperature T_{ex} can then be derived easily from the equation of radiative transfer:

$$T_{mb} = [J_\nu(T_{ex}) - J_\nu(T_{bg})]\,[1 - \exp(-\tau)], \quad (2)$$

where we assumed a unity filling factor and $T_{bg} = 2.7$ K. In Eq. (2) we also used $J_\nu(T) \equiv T_o/[\exp(T_o/T) - 1]$, with $T_o = h\nu/k$, where h and k represent the Planck and Boltzmann constants, respectively.

Given T_{ex} and τ_{13} for the $J = 1{-}0$ transition, the total column density, N_{mol}, of ^{13}CO can be derived using the following formula (see, e.g., Lis & Goldsmith 1991):

$$N_{mol}\,[cm^{-2}] = \frac{4.0\times10^{12}}{J^2\mu^2[D]\,B[K]} Z \exp\left(\frac{E_J}{T_{ex}}\right) \times \frac{1}{\eta_{mb}}\frac{\tau}{1-e^{-\tau}}\int T_A^\star\,dv\,[K\ km\ s^{-1}], \quad (3)$$

where B denotes the rotational constant, E_J is the upper state energy, μ is the dipole moment (in Debye) and we used the escape probability $\tau/[1-\exp(-\tau)]$ to account for first-order optical depth effects. With Z we have indicated the partition function of a linear molecule which, for $kT_{ex} \gg hB$, is given by:

$$Z = \frac{kT_{ex}}{hB}. \quad (4)$$

The molecular hydrogen column density, $N(H_2)$, was then calculated assuming a $[^{13}CO]/[H_2] \simeq 1.4\times10^{-6}$ abundance ratio (Frerking et al. 1982) and thus we obtain $[C^{18}O]/[H_2] \simeq 2\times10^{-7}$. The top panel of Fig. 5 shows the resulting column density map at all positions where both T_{ex} and τ_{13} could be reliably calculated. The column density and Hi-GAL 250 μm emission maps look quite similar, with the notable exception of the enhanced 250 μm emission at position (RA, Dec) $\simeq$ (07:10:05, −10:32:00) which has no corresponding clump in the $N(H_2)$ map. This may be a consequence of $C^{18}O$ not tracing closely the dust emission at this position (see Sect. 3.2) and also because of the partially missing data near this position as well (see Figs. 2 and A.2). The missing data near the peaks of $N(H_2)$ are due to the ^{13}CO line becoming self-absorbed and the ratio R becoming <1. The typical values for excitation temperature and opacity across the measured region are $T_{ex} \sim 5{-}9$ K and $\tau_{13} \sim 2{-}10$. This suggests that the ^{13}CO line is mostly optically thick, but also the $C^{18}O$ line could be moderately optically thick at some positions.

4.1.2. Results from the ^{12}CO and ^{13}CO data

The ^{13}CO and $C^{18}O$ data are effective in deriving excitation temperature, opacity and column density along the main filament. However, as shown by Fig. 5, there are regions in the map where the physical parameters of the gas could not be determined, mainly because the $C^{18}O$ spectra were not good enough. We then decided to use ^{12}CO and ^{13}CO to extend the derivation of the physical parameters to most of the field area mapped with the Mopra telescope.

Then, assuming that the ^{12}CO transition is optically thick and that $T_{pk}[^{12}CO]$ is the main beam brightness temperature at the peak of $^{12}CO(1{-}0)$, we can derive the excitation temperature using Eq. (2):

$$T_{ex} = \frac{T_o[^{12}CO]}{\ln[1 + T_o[^{12}CO]/(T_{pk}[^{12}CO] + 0.86K)]}, \quad (5)$$

where $T_o[^{12}CO] = h\nu[^{12}CO]/k = 5.5$ K.

Then, assuming that the excitation temperatures of the ^{12}CO and ^{13}CO lines are the same, the optical depth of ^{13}CO can also be derived from Eq. (2):

$$\tau[^{13}CO] = -\ln\left[1 - \frac{T_{pk}[^{13}CO]/T_o[^{13}CO]}{1/(\exp(T_o[^{13}CO]/T_{ex}) - 1) - 0.16}\right], \quad (6)$$

where $T_o[^{13}CO] = h\nu[^{13}CO]/k = 5.3$ K and $T_{pk}[^{13}CO]$ is the main beam brightness temperature at the peak of ^{13}CO. The main *caveat* of this method is that the most dense regions will not be accurately probed by ^{12}CO, whose emission is restricted to outer cloud material due to its higher opacity. The bottom panel of Fig. 5 shows the resulting column density. The discrepancies with respect to the column density map obtained as described in Sect. 4.1.1 are clearly visible, and they are likely a consequence of the assumptions made for each method, in particular regarding the molecular abundances. We also note that the values for the H_2 column density obtained by Elia et al. (2013) using the dust continuum emission are typically intermediate between those shown in the lower and upper panels of Fig. 5, indicating an overall internal consistency.

4.2. Gas kinematics

4.2.1. Velocity gradients

Systematic variations in the ^{13}CO and $C^{18}O$ line center velocity are apparent across the mapped region. In fact, it can be seen in Figs. 6 to 8 that the velocity gradually increases along a particular direction.

We measure the velocity gradient across the whole mapped region following the procedure outlined in Goodman et al. (1993). We assume the centroid velocities of the spectral lines follow a simple linear form and fit the function:

$$V_{lsr} = V_o + a\,\Delta\alpha + b\,\Delta\delta, \quad (7)$$

to the peak velocity of a Gaussian fit to the emission profile of the ^{13}CO and $C^{18}O$ lines. Here, $\Delta\alpha$ and $\Delta\delta$ represent offsets in right ascension and declination, expressed in radians, a and b are the projections of the gradient per radian on the α and δ axes, respectively, and V_o is the LSR systemic velocity of the cloud.

We found the best-fitting values to the constants a and b using `MPFIT` (Markwardt 2009), and then converted all of the angular velocity gradients to physical scale assuming a distance of 1 kpc. This yields the overall velocity gradients listed in Table 1. Since in the Gaussian fitting procedure only spectra with a $S/N \geq 4$ are considered, the velocity gradient estimated from $C^{18}O$ is mainly sensitive to systematic variations along the main filament, while the velocity gradient estimated from ^{13}CO is sensitive to velocity variations across the whole mapped region. This may explain the higher value of dV/dr derived from $C^{18}O$. In Table 1 the velocity gradient from $C^{18}O$ along the secondary filament has not been estimated because we have few spectra with $S/N \geq 4$.

The V_o and θ_v parameters of the best-fit velocity gradients are quite similar for both molecular tracers. The values estimated

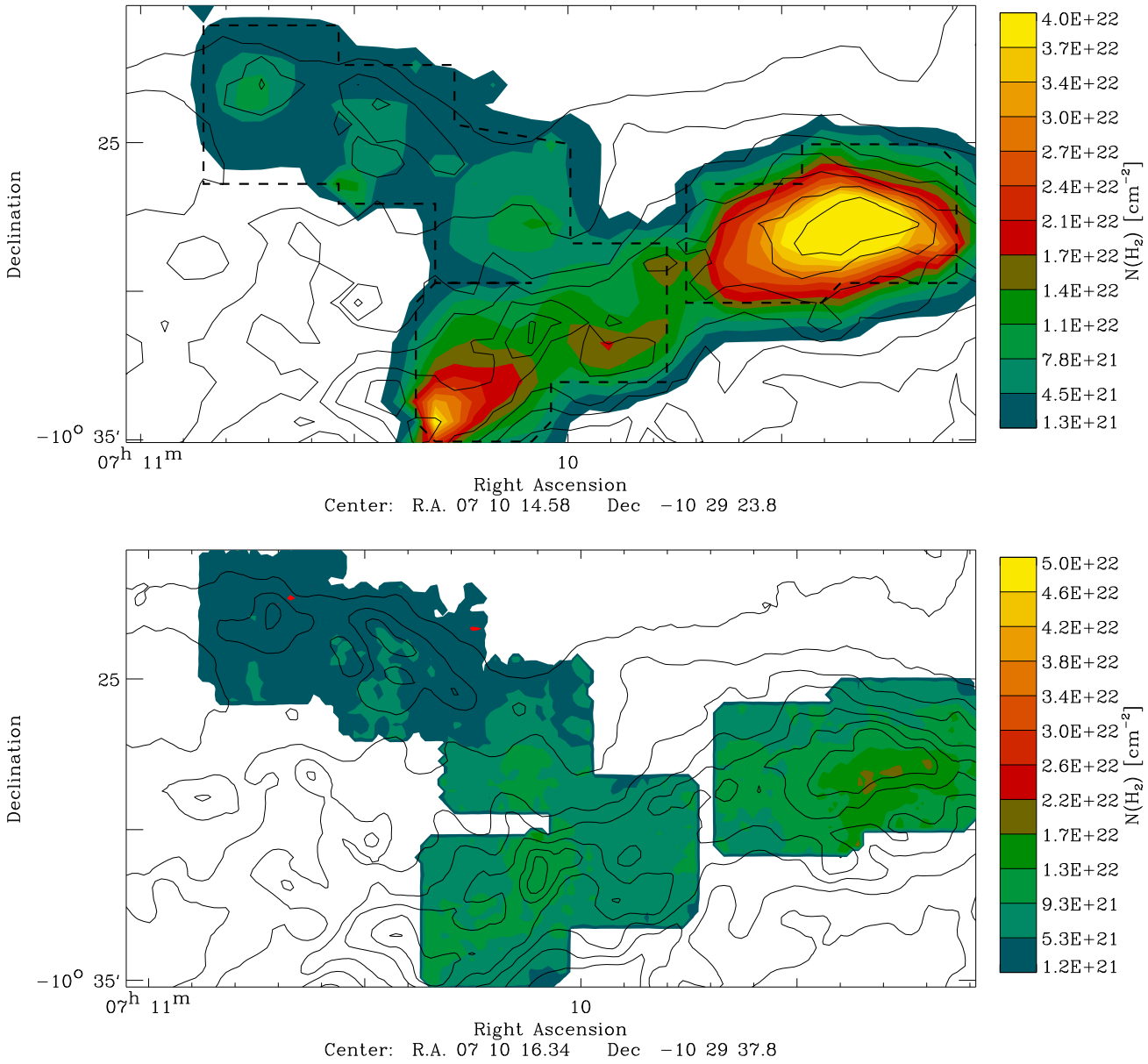

Fig. 5. H_2 column density map as derived from the ^{13}CO and C^{18}O(1−0) data, regridded with the program `xs` to a 80 arcsec grid size and 40 arcsec spacing (*top panel*), and from the ^{13}CO and ^{12}CO(1−0) data (*bottom panel*). Overlaid are the contours of the column density as derived by Elia et al. (2013) (with first contour corresponding to 2.8×10^{21} cm^{-2} and subsequent contours equally spaced on a logarithmic scale, with Log(ΔN[cm^{-2}]) = 0.2), which are also regridded in the top panel. Abundance ratios of [^{13}CO]/[C^{18}O] ≃ 7 and [C^{18}O]/[H_2] ≃ 10^{-7} were assumed (see text).

Table 1. Results of velocity gradient fitting.

Line	Whole region[a]			Main filament			Secondary filament		
	V_o	dV/dr	θ_v[b]	V_o	dV/dr	θ_v[b]	V_o	dV/dr	θ_v[b]
	[km s^{-1}]	[km s^{-1} pc^{-1}]	[deg]	[km s^{-1}]	[km s^{-1} pc^{-1}]	[deg]	[km s^{-1}]	[km s^{-1} pc^{-1}]	[deg]
C^{18}O (1−0)	15.1	0.42	292	15.3	0.35	318	–	–	–
^{13}CO (1−0)	14.9	0.25	293	15.2	0.30	311	15.2	0.35	279

Notes. [a] Including the isolated region in the SE. [b] The angle θ_v is measured positive from the axis of positive RA toward the north.

from ^{13}CO show that the directions of the velocity gradient along the main and secondary filament are clearly different, by more than 30 deg. In particular, the velocity gradient along the main filament is oriented almost parallel to the filament itself, with velocity increasing roughly from the NE to the SE, as also shown by Figs. 6 and 7. The velocity gradient associated with the secondary filament appears instead almost perpendicular to the filament itself. However, this result is less reliable because of the limited extent of the mapped region, especially in the direction orthogonal to the filament.

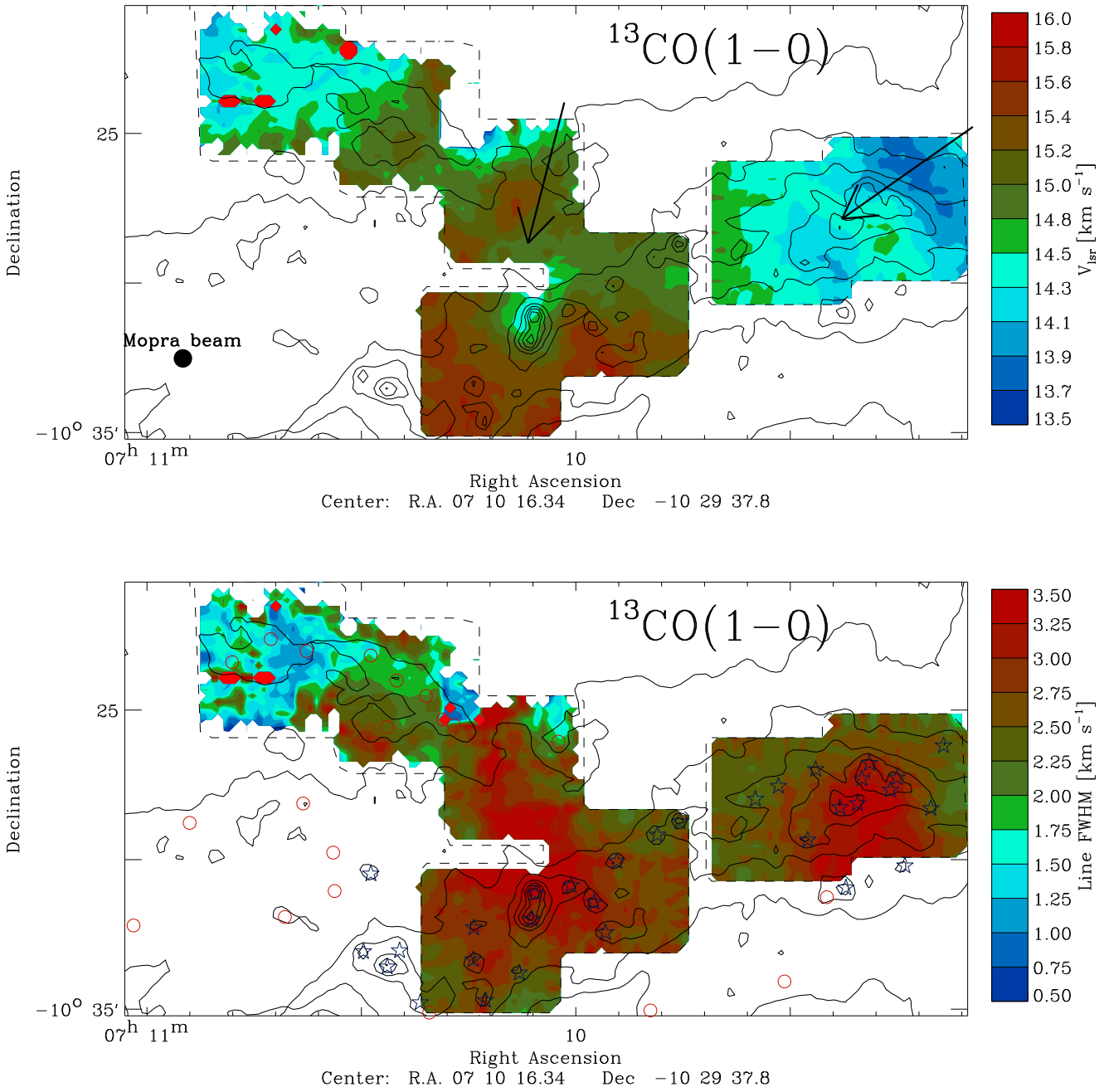

Fig. 6. Kinematics toward the $\ell = 224°$ region. The *top panel* shows the line center velocity from the ^{13}CO(1−0) data, while the *bottom panel* shows the line width. The black arrows represent the direction and relative magnitude of the velocity gradients along the main and secondary filaments (see Sect. 4.2.1), while the black filled circle at the bottom left (*top panel*) indicates the Mopra beam FWHM. Symbols in the *lower panel* are as in Fig. 1. The overlaid contours of the SPIRE 250 μm emission are as in Fig. 5. The line centers and line widths have been computed by fitting a 1- or 2-component Gaussian to the spectrum at each point (see text).

In Sect. 5.3 we suggest that a possible physical cause for the observed velocity gradients is the presence of accretion flows. However, at present we cannot exclude that the observed velocity gradients are produced by other motions. For example, the velocity gradients could be interpreted as rotation, though our limited and irregular mapped area makes this interpretation more difficult. Then following Goodman et al. (1993) we can calculate the parameter β, defined as the ratio of rotational kinetic energy to gravitational energy for a sphere of uniform density $\delta_\circ$:

$$\beta = \frac{\omega^2}{4\pi G \delta_\circ}, \quad (8)$$

where ω is the angular velocity and G is the gravitational constant. For the most intense region of emission in the NW section of the main filament (shown as a black box in Fig. 2) we find $\beta \simeq 0.08$, suggesting that if this interpretation were correct then the rotational energy would be a negligible fraction of the gravitational energy.

At present, we do not have data indicating the presence of protostellar outflows in the mapped region. However, while outflows could be a plausible physical explanation for velocity gradients observed at the clumps scale, it is unlikely that a single outflow or multiply oriented outflows could explain the observed large-scale velocity gradients.

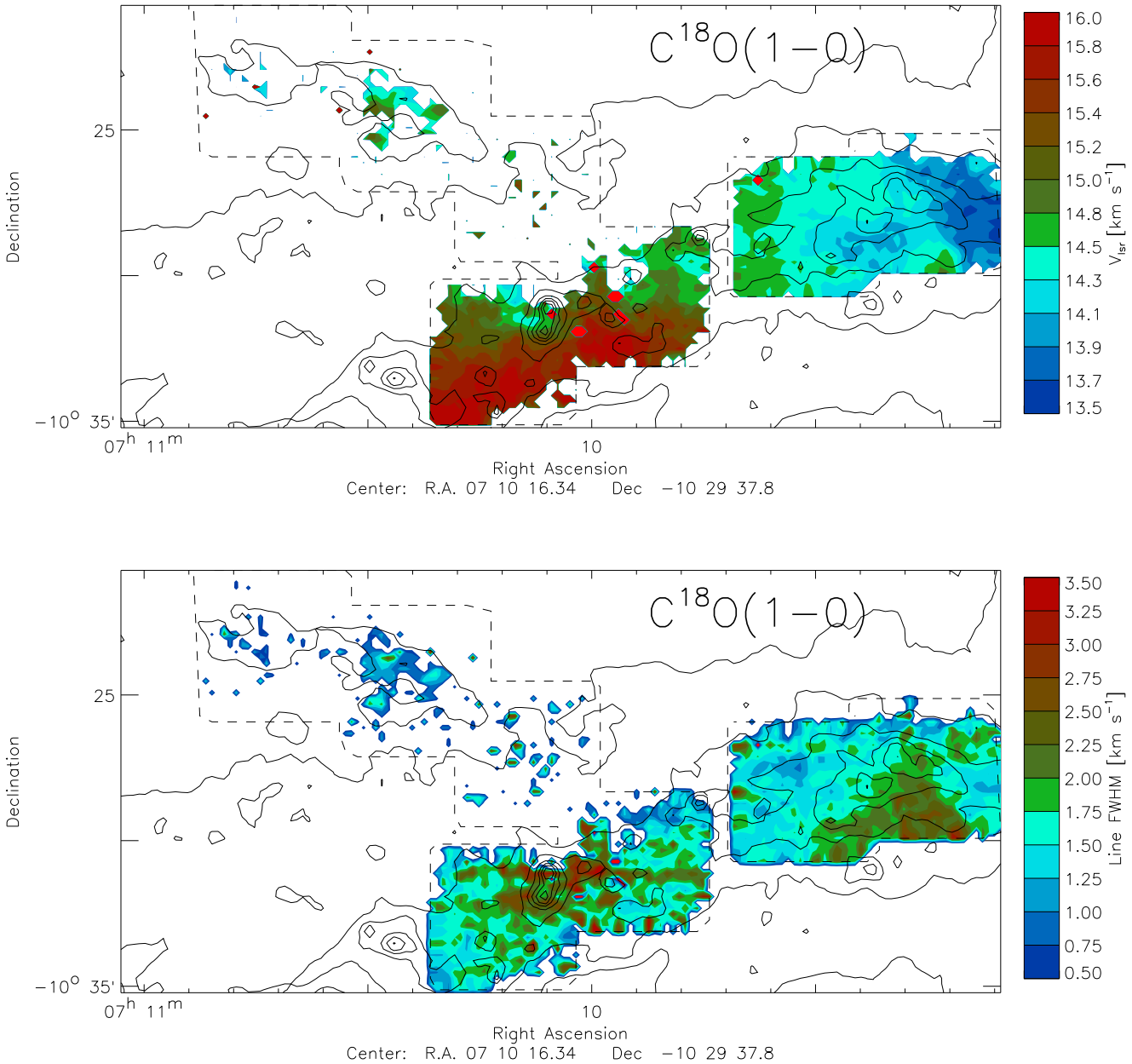

Fig. 7. Same as Fig. 6 for $C^{18}O(1-0)$. The line centers and line widths have been computed by fitting a 1-component Gaussian to the spectrum at each point (see text).

4.2.2. Line profile and line widths

Figures 1 and 5 show a reasonable agreement between the distributions of dust emission and gas column density. Figure 1 also shows that the Hi-GAL compact clumps concentrate in regions of higher column density relative to the surrounding regions, as expected. Figures 6 and 7 then show that on the main filament the column density roughly correlates also with the $C^{18}O$ and ^{13}CO velocity dispersion. However, Fig. 6 shows that on the secondary filament such a correlation is much less evident, and actually looks like an anti-correlation at some positions.

Likewise, Figs. 6 to 8 show that starless clumps are preferentially located at positions where the line widths are generally lower than those observed at the positions of the protostellar clumps. This is confirmed by extracting the $C^{18}O$ line width at the nominal position of each Hi-GAL clump, if the line was detected. Table 2 then shows the average line widths as measured from the $C^{18}O$ spectral line cube at the original angular resolution (column "Clump center"), and also the average values after the cube has been spatially convolved (regridded with the program `xs` to a 80 arcsec grid size and 40 arcsec spacing). The latter values (column "Ambient gas") are more representative of the molecular gas surrounding the clump, and should give a better estimate of the kinematical status of the ambient gas immediately around the Hi-GAL clump. Table 2 shows that in both case the $C^{18}O$ line widths are larger toward the protostellar clumps, though they are marginally consistent within the errors. The location of starless clumps in regions of lower velocity dispersion is further confirmed by the small linewidths measured in the isolated tile at the SE (see Fig. 8), which hosts a small cluster of starless clumps.

Our analysis shows evidence of gas flow along the main filament. However, we do not find any signs of accretion flow from the filament onto the Hi-GAL clumps. In fact, as mentioned

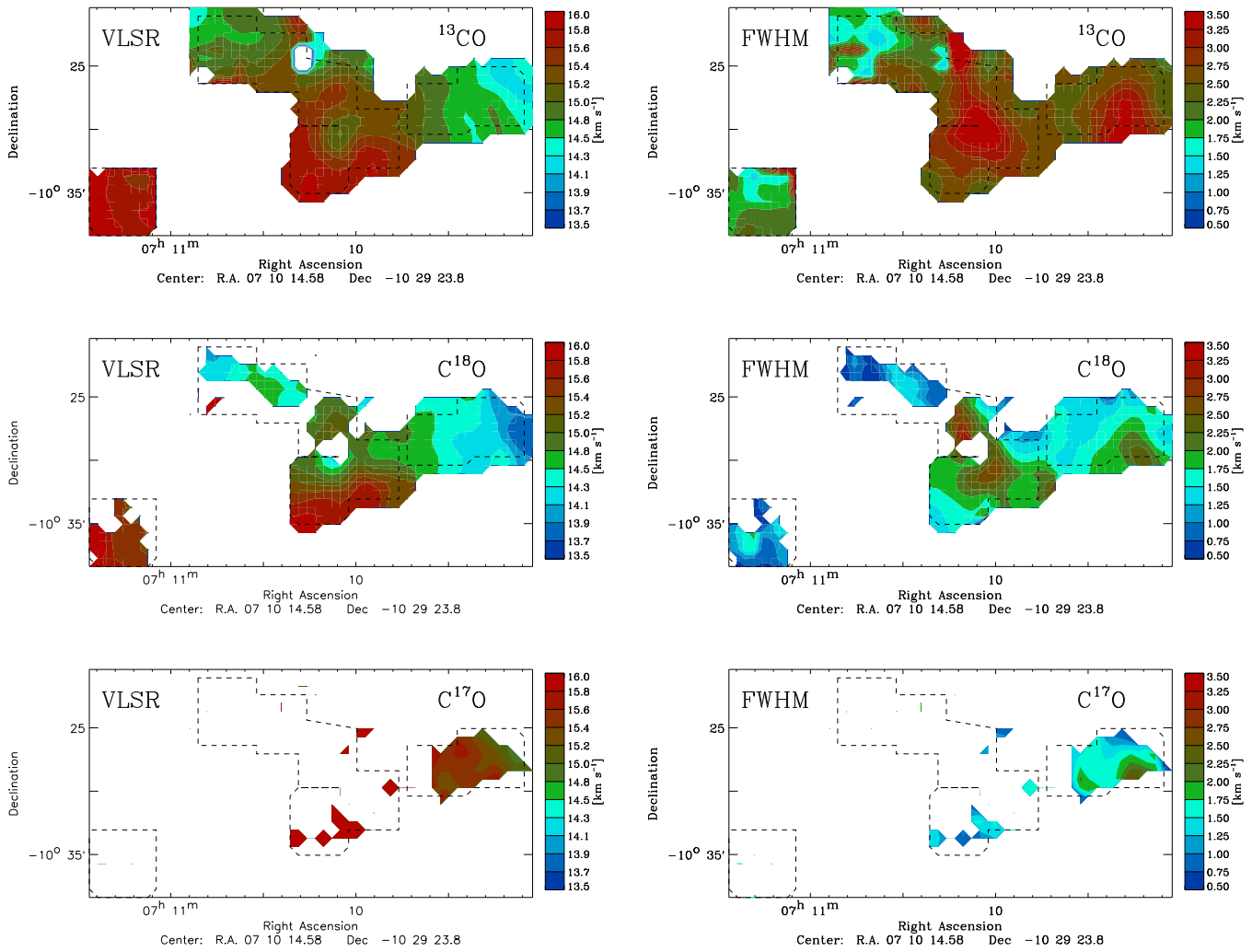

Fig. 8. Line center velocities (*left column*) and line widths (*right column*) after convolving (*from top to bottom*) the ^{13}CO, C^{18}O and C^{17}O(1–0) Mopra maps to 80″ and regridding with a 40″ spacing. The smaller red areas are map artifacts.

Table 2. Line FWHM of the molecule of mean mass toward the Hi-GAL clumps (see Sect. 4.3.2).

Clump type	Clump center [km s^{-1}]	Ambient gas [km s^{-1}]
Starless	1.3 ± 0.3	1.4 ± 0.5
Protostellar	1.8 ± 0.5	1.9 ± 0.3

in Sect. 3.3 the line profiles of our emission lines are mostly Gaussian and double-peaked in some cases, and we do not observe clear signs of self-absorption. The lack of (detectable) self-absorption means that we do not see any sign of infall or gas accretion across the filaments. Self-absorbed line profiles in filamentary regions were instead observed, for example, toward the Serpens South cluster and filament (Kirk et al. 2013) and also toward the high-mass star-forming region DR21 (Schneider et al. 2010), where evidence for material radially contracting onto the filaments has been found. In these two regions the authors used the HCO$^+$ (1–0) line to detect and analyze the self-absorption. However, Arzoumanian et al. (2013) did not detect any sign of self-absorption in their observations of C^{18}O (1–0), (2–1) and ^{13}CO (2–1) toward several filaments. Clearly, the exact line profiles of HCO$^+$, C^{18}O and ^{13}CO depend on the velocity and density structure of both the ambient gas and the molecular clumps. Carrying out a detailed comparison of the line profiles of these different molecular tracers is beyond the scope of this paper. However, even without using complex radiative transfer codes, it is possible to analyze the effects of various source and telescope parameters on the hypothetical blue-asymmetric infall line profile using an analytical model, such as the one discussed by De Vries & Myers (2005).

Another parameter of interest for the analysis of the Hi-GAL clumps is the non-thermal (turbulent) component of the velocity line widths. If we take a clump's observed velocity line width, $\Delta V_{\mathrm{C^{18}O}}$, to be the quadrature sum of its thermal and non-thermal line widths (assuming that the two contributions are independent of each other), ΔV_{T} and ΔV_{NT}, respectively:

$$\Delta V^2_{\mathrm{C^{18}O}} = \Delta V^2_{\mathrm{T}} + \Delta V^2_{\mathrm{NT}}, \tag{9}$$

then in order to find ΔV_{NT} we must determine ΔV_{T}:

$$\Delta V^2_{\mathrm{T}} = 8 \log 2 \frac{kT}{m_{\mathrm{C^{18}O}}}, \tag{10}$$

where $m_{\mathrm{C^{18}O}}$ is the mass of the C^{18}O molecule. The clump temperature, $T = T_{\mathrm{d}}$, is taken from the dust-determined Hi-GAL

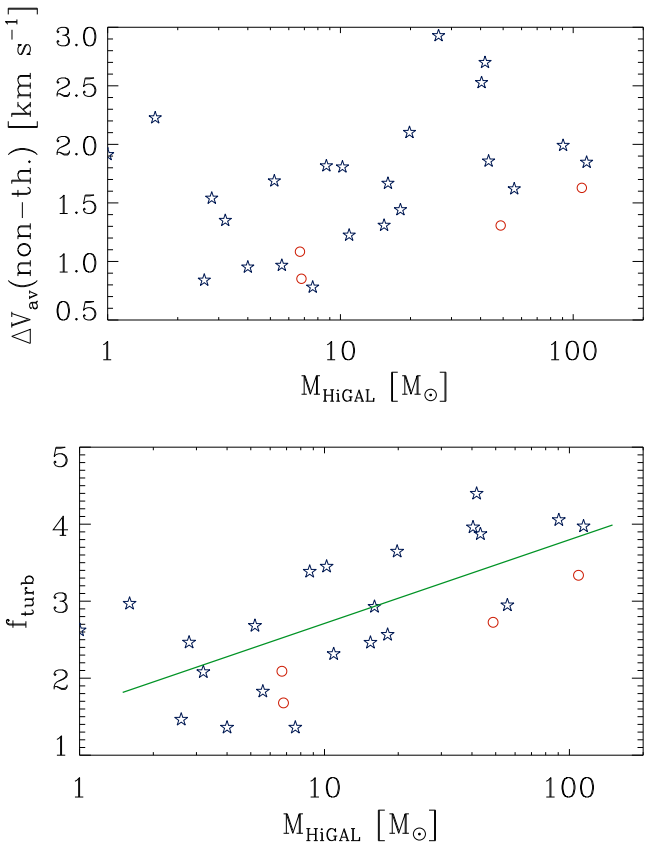

Fig. 9. *Top panel*: non-thermal component of the velocity line width of the $C^{18}O$ (1−0) transition, vs. the total clump mass, $M_{clump} = M_{HiGAL}$ (see text). Stars represent protostellar clumps and the empty circles represent starless clumps. *Bottom panel*: non-thermal velocity dispersion, from $C^{18}O$ (1−0), to sound speed ratio, f_{turb}, vs. the total clump mass, M_{clump}. The green solid line represents the linear fit to all points (see text); the Spearman rank coefficient is 0.66.

physical parameters. The top panel of Fig. 9 shows ΔV_{NT}, estimated for all Hi-GAL clumps with a reliable $C^{18}O$ detection, vs. the total clump mass, $M_{clump} = M_{HiGAL}$, also derived from the Hi-GAL data. This figure shows a tentative trend of increasing ΔV_{NT} with M_{clump} and, despite the low number of starless clumps in this plot, it also shows that ΔV_{NT} tends to be higher toward protostellar clumps. The average values of ΔV_{NT} are 1.2 ± 0.3 km s^{-1} and 1.7 ± 0.6 km s^{-1} for starless and protostellar clumps, respectively.

However, because of the difference in temperature, the physically significant parameter is the non-thermal velocity dispersion, σ_{NT}, to thermal sound speed, c_s, ratio which we call $f_{turb} = \sigma_{NT}/c_s$ following Curtis & Richer (2011). $c_s = \sqrt{(\gamma kT/m_{av})}$ is the isothermal sound speed in the bulk of the gas of mean molecular weight $m_{av} = 2.3$ amu (with respect to the total number of particles), assuming a mass fraction for He of 25%. The parameter γ is the adiabatic index (≃7/5 for a diatomic molecular gas). In the bottom panel of Fig. 9 we then plot f_{turb} vs. M_{clump}, and we note that the trend of increasing f_{turb} with mass is still visible. We also note that for similar ranges of mass the f_{turb} parameter of the starless clumps is typically lower compared to that of protostellar clumps, though their (full range) average values are 2.46 ± 0.73 and 2.96 ± 1.02, respectively. In the bottom panel of Fig. 9 we also show the result of a linear regression to find the slope of the best fit line, using the Bayesian IDL routine `LINMIX_ERR`.

Our results clearly indicate that the line widths toward the Hi-GAL clumps are supersonic. In addition, since stars can inject significant energy into their surroundings, it is not surprising that protostellar clumps display somewhat larger non-thermal velocity dispersion compared to starless clumps, within similar mass ranges. Instead, Curtis & Richer (2011) do not find a significant difference between the distributions of f_{turb} of the starless and protostellar subsets. Clearly, we need similar samples of starless and protostellar clumps in order for these differences to be statistically significant.

4.3. Derivation of masses

4.3.1. Mass of the filaments derived from column density

The calculation of the filaments mass from the column density assumes LTE and we determine the molecular gas mass integrating the molecule column density over a given extent of the molecular cloud. Then we can write:

$$M_{cd} = d^2\, m_{mol} \int N_{mol}\, d\Omega, \tag{11}$$

where $\int N_{mol}\, d\Omega$ is the molecule column density integrated over the region enclosed by the chosen contour level, m_{mol} is the mass of the specific molecule being considered, and d is the distance to the source. Equation (11) is actually implemented by writing:

$$M_{cd} = d^2\, m_{mol}\, \Delta\Omega_{pix} \sum_{i=1}^{n_{pix}} N_{mol}(x_i, y_i), \tag{12}$$

where $N_{mol}(x_i, y_i)$ represents the column density in a single pixel (x_i, y_i) of the map, with n_{pix} representing the total number of pixels, and $\Delta\Omega_{pix}$ represents the solid angle covered by a single pixel. The map pixels selected are those that have an integrated intensity $I \geq 3\sigma_{map}$, where the RMS integrated intensity, $\sigma_{map} \simeq 0.2$ K km s^{-1}, has been estimated directly from the map, averaging pixels where no emission is detected.

Using the H_2 column density derived from the ^{13}CO and ^{12}CO(1−0) lines (shown in the bottom panel of Fig. 5) the total gas mass calculated is $\sim 2.5 \times 10^3\, M_\odot$, including the isolated tile shown in Fig. 1, using the relative molecular abundances described in Sect. 4.1. Specifically, we obtain $\simeq 1.8 \times 10^3\, M_\odot$ and $\simeq 6.0 \times 10^2\, M_\odot$ for the main and secondary filaments, respectively. For comparison, if we use the H_2 column density derived from the ^{13}CO and $C^{18}O$(1−0) lines (shown in the top panel of Fig. 5) the total gas mass calculated would be $\sim 4.4 \times 10^3\, M_\odot$.

4.3.2. Clumps virial mass

The question of whether molecular clumps and their substructures are bound is of great importance in understanding star and cluster formation. The virial mass estimate, in combination with other mass estimates, may allow to determine whether or not a specific clump is bound and virialized. We estimate the virial mass of the clumps assuming they are simple spherical systems with uniform density (MacLaren et al. 1988):

$$M_{vir}[M_\odot] = 210\, R_{dec}[\mathrm{pc}]\, (\Delta V_{av}[\mathrm{km\ s^{-1}}])^2, \tag{13}$$

where R_{dec} is the deconvolved source radius and ΔV_{av} represents the line FWHM of the molecule of mean mass, calculated as the sum of the thermal and turbulent components (see Sect. 4.2.2):

$$\Delta V_{av}^2 = \Delta V_{mol}^2 + kT\, 8 \ln 2 \left(\frac{1}{m_{av}} - \frac{1}{m_{mol}}\right), \tag{14}$$

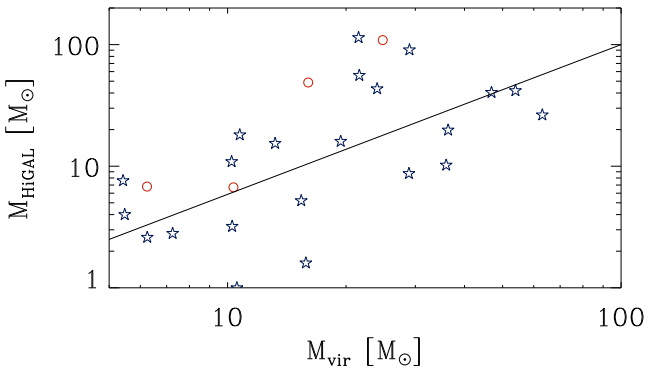

Fig. 10. Total clump mass, $M_{\rm clump} = M_{\rm HiGAL}$, vs. the virial mass, $M_{\rm vir}$, calculated using the velocity line widths of the $C^{18}O$ (1–0) transition (see text). The solid line indicates the minimum $M_{\rm clump} = 0.5\,M_{\rm vir}$ for which the clump should be self-gravitating. Symbols are as in Fig. 9.

where $\Delta V_{\rm mol}$ is the line FWHM of the molecular transition being considered. We note that according to MacLaren et al. (1988), Eq. (13) may lead to a mass overestimate if the density distribution is not uniform. For example, in the case of a sphere with a density distribution $\rho \propto r^{-2}$ the numerical factor in Eq. (13) should be replaced by 126.

As described in Sect. 4.2.2 the line FWHM is calculated from the $C^{18}O$ spectrum observed at the nominal position of each Hi-GAL clump. Since even $C^{18}O$ may not trace the denser molecular gas and may be affected by the ambient, less dense material, we have corrected its line width for the average ratio of the $C^{17}O$ to $C^{18}O$ line width ratio, which is 0.84 toward the bright region of emission in the NW section of the main filament (shown as a black box in Fig. 2). In addition, we have used the numerical factor 126 in Eq. (13), since for the density profiles of molecular clumps power-laws have been put forward by various studies (see, e.g., Fontani et al. 2002 where they find $n \sim r^p$ with an average $p = -2.59$).

The plot of the total clump mass, $M_{\rm HiGAL}$, as derived from Hi-GAL, vs. the virial mass is shown in Fig. 10. We note that all of the starless clumps where the $C^{18}O$ line has been detected lie above the self-gravitating line, indicating that they are likely to be gravitationally bound. The protostellar clumps, much more numerous, are almost equally divided between those above and below the self-gravitating line. In interpreting this plot, however, one should consider that the line widths we measure are from a region (determined by the Mopra telescope beam) that is generally different than the virial radius we assign to it, which is instead determined from the source-extraction procedure used for the Hi-GAL maps. Whether the continuum emission is more extended or not than the dense molecular gas emitting volume depends on the specific excitation conditions of the gas and the molecular tracer. Therefore, given the uncertainties in both the virial and Hi-GAL dust mass estimates, it is not possible to draw unequivocal conclusions about the stability of individual clumps.

4.3.3. Dust continuum masses

Obtaining mass estimates of molecular clouds with molecular lines may be problematic due to high column densities and also molecular freezeout onto dust grains in some cases. Alternatively, the cold dust emission, as observed in the (sub)millimeter, can be used to provide more reliable mass estimates as it is optically thin and does not deplete.

We use the 250 μm dust continuum emission from Hi-GAL, to achieve isothermal mass estimates using the expression:

$$M_{\rm cont} = \frac{I_\nu\, d^2}{r\, k_{250}\, B_\nu(T_{\rm d})}, \tag{15}$$

where I_ν is the source surface brightness (or specific intensity) in the Hi-GAL map at 250 μm (MJy sr^{-1}), d is the distance (cm), $r\,k_{250}$ is the dust mass absorption coefficient (cm^2 g^{-1}), often called the opacity, corrected for the dust-to-gas ratio, r, at $\lambda_\circ = 250\,\mu$m, and $B_\nu(T_{\rm d})$ is the Planck function at dust temperature, $T_{\rm d}$. We adopt a value of $r\,k_{250} = 0.11$ cm^2 g^{-1} from Martin et al. (2012).

We integrate I_ν in the same area as mapped at Mopra, as shown in Fig. 1, and also assume that $T_{\rm d}$ can vary in the same range analyzed by Martin et al. (2012), that is, $\simeq$12–17 K. We then obtain $M_{\rm cont} \sim 2 \times 10^3\,M_\odot$ ($T_{\rm d} = 12$ K) and $M_{\rm cont} \sim 5 \times 10^2\,M_\odot$ ($T_{\rm d} = 17$ K). If we use a typical intermediate value of $T_{\rm d} = 14$ K, the total mass is $M_{\rm cont} \sim 10^3\,M_\odot$ and specifically, $M_{\rm cont} \sim 7.6 \times 10^2$ and $\sim 1.9 \times 10^2\,M_\odot$ for the main and secondary filaments, respectively. Given all uncertainties in both molecular abundances and dust parameters, the dust continuum masses agree reasonably well with the column density masses derived in Sect. 4.3.1. Also the main to secondary filament mass ratios estimated from molecular lines and dust continuum are very similar ($M_{\rm main}/M_{\rm sec} \simeq 3$–4), showing that the secondary filament has about 1/3 of the mass of the main filament. The good agreement of the mass ratio, $M_{\rm main}/M_{\rm sec}$, derived with these two methods, suggests that the difference between the absolute mass values, $M_{\rm main}$ and $M_{\rm sec}$, derived from the molecular lines and the dust continuum depends on the choice of parameters such as molecular abundances and dust mass absorption coefficient.

5. Discussion

The results presented in Sects. 3 and 4 can be used to discuss the physical properties and evolutionary state of the two filaments.

5.1. Column density profiles

In this section, we analyze the radial column density profile of the filaments using both molecular line emission and dust submillimeter continuum emission. To construct the mean radial density profile of each filament we used the following procedure. First, we searched for the location of peak emission along every cut in declination through each filament. A simple scanning in declination allowed us to unambiguously find the peak emission because the main axis of each filament make a large (>45°) angle to the declination axis. Second, we constructed the midline of each filament by joining all peak ridge points. We then measured a radial column density profile perpendicular to the midline at each position. Finally, we derived the mean radial profile by averaging all profiles along each filament. The mean profiles and standard deviations, at each radial separation, are shown in Fig. 11.

In order to characterize each observed column density profile, following Arzoumanian et al. (2011) we adopt the model of a cylindrical filament with radial column density profile (as a function of cylindrical radius r) of the form:

$$N_{\rm H_2}(r) = A_{\rm p}\, \frac{\rho_{\rm c} R_{\rm flat}}{[1 + (r/R_{\rm flat})^2]^{\frac{p-1}{2}}}, \tag{16}$$

where $N_{\rm H_2}(r)$ is the column density at radial separation r, $\rho_{\rm c}$ is the number density at the center of the filament, $R_{\rm flat}$ is the characteristic radius of the flat inner portion of the density profile,

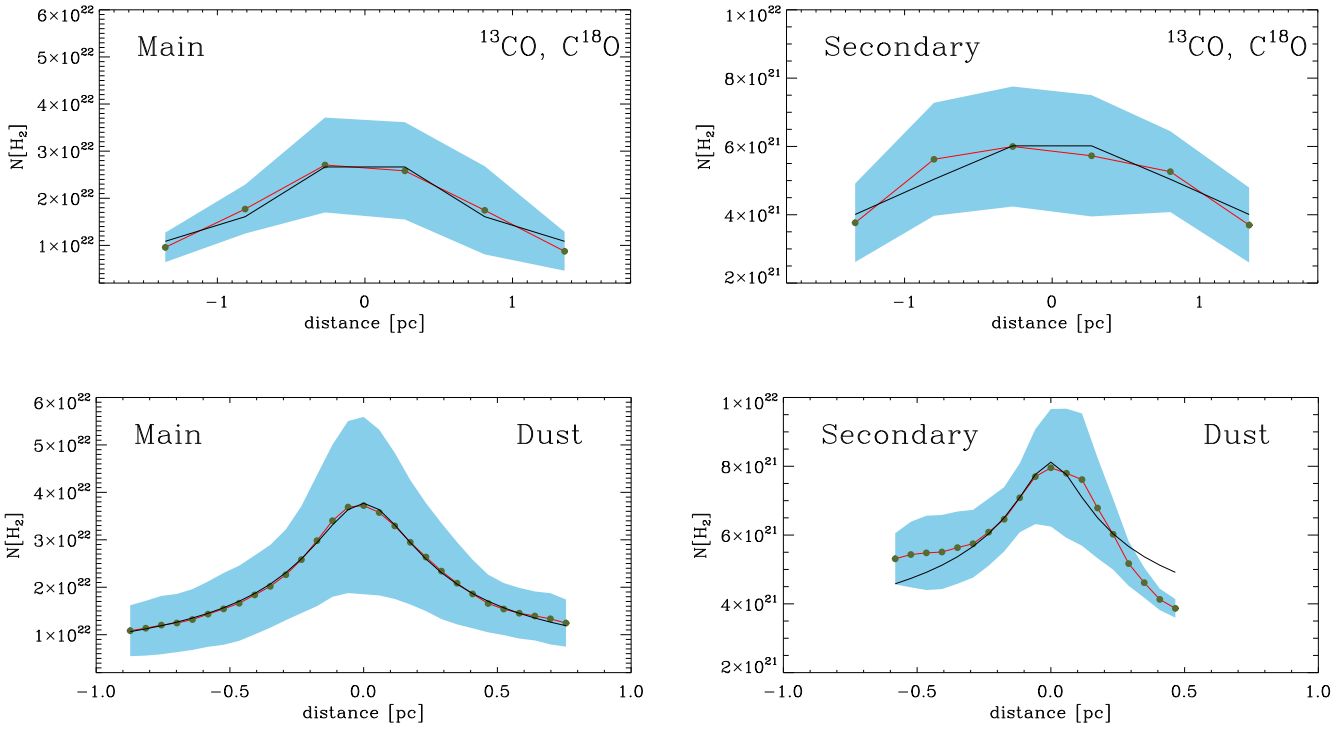

Fig. 11. Radial column density profile of the main (*left column*) and secondary (*right column*) filaments. The dots, connected by the red solid line, show the mean profile across the filaments, while the shaded area indicates the standard deviation. In the top row the average profiles were estimated from the ^{13}CO and C^{18}O(1−0) derived column density (Fig. 5, top panel), while in the bottom row we used the column density estimated by Elia et al. (2013). The black solid line represents the best fit profile, following the formulation in Arzoumanian et al. (2011).

Table 3. Parameters corresponding to the best-fit model of the form expressed by Eq. (16) to the mean column density profile of the main and secondary filaments.

Filament	Main filament			Secondary filament		
	ρ_c	R_{flat}	p	ρ_c	R_{flat}	p
	[$\times 10^5$ cm^{-3}]	[pc]		[$\times 10^5$ cm^{-3}]	[pc]	
Spectral lines	0.6	0.48	1.9	–	–	–
Dust emission	1.8	0.19	1.8	0.3	0.10	1.3

and the parameter A_p, for $p > 1$, is calculated as:

$$A_p = \frac{1}{\cos i} \int_{-\infty}^{\infty} \frac{du}{(1+u^2)^{p/2}}, \quad (17)$$

where the inclination angle along the line of sight, i, is assumed to be 0 for simplicity. Allowing all three parameters, p, ρ_c and R_{flat} to vary, we find the values listed in Table 3, while the best fit profiles are shown in Fig. 11. For the dust continuum emission we used the column density map derived by Elia et al. (2013) for better accuracy. In fact, they obtained the column density after performing a fit to the SED at each point in the Hi-GAL maps, thus deriving the dust temperature at the same time.

Comparing the best-fit values of Table 3 with those in the literature, we find that the values of p are similar to those found by Arzoumanian et al. (2011) and André et al. (2016, who used dust derived column density maps), and also by Kirk et al. (2013, who used molecular lines). However, Nutter et al. (2008) found a value of p somewhat higher ($p = 3$) toward TMC1. Instead, the best fit values of the other two free parameters, ρ_c and R_{flat}, significantly differ from those of Kirk et al. (2013), Arzoumanian et al. (2011, who do not list their ρ_c values) and André et al. (2016), particularly when the values derived from the molecular lines are considered. However, our best-fit values for all three parameters are quite similar to those found by Juvela et al. (2012b), who in addition analyzed sources with a range of distances more similar to that of the $\ell = 224°$ region, and hence with similar distance-related effects.

The differences found in the literature are certainly caused, at least in part, by the way the analyzed structures are selected and by the analysis methods themselves (see for example the discussion in Juvela et al. 2012b). Specifically, although both of the filaments studied here have been identified by Schisano et al. (2014), they are not as well defined (e.g., with a sharper central peak in the column density average profile) as those mapped by Kirk et al. (2013) and Arzoumanian et al. (2011), which also lie at quite a different distance, or also simulated (see, e.g., Juvela et al. 2012a). It is not thus entirely surprising that we obtain lower values of the filament central density and a higher value of R_{flat}.

In Table 3 and Fig. 11, comparing the column density profiles obtained from the molecular lines and from the dust continuum emission, the observed discrepancies are likely caused in part by the different radial extent measurable in the Mopra and Hi-GAL maps. In fact, when using the column density derived from

molecular line emission the reliability of our fit is limited by the fact that we were able to measure the radial column density profile only relatively close to the central ridge. For the specific case of the secondary filament, the radial column density profile from the Mopra data is more uncertain due to the lower S/N in this region of the map, particularly at the edges of the filament, and thus the best-fit parameters are not shown in Table 3. The main filament should be less affected by S/N problems and the different radial profiles shown in Fig. 11 must thus be caused also by the method used to retrieve the column density and/or the intrinsic distribution of the material detected with each technique. The shallow or flat radial column density profile derived from the Mopra spectral line data suggests that we are probably sensitive to some amount of large-scale structures, that is, diffuse material not directly associated with the star-forming regions along the filament, which is more reliably traced by the optically thin dust emission.

5.2. Gravitational stability of the filaments

The properties of interstellar filaments and possible scenarios for their formation and evolution have already been discussed in many papers, both theoretically (e.g., Ostriker 1964; Inutsuka & Miyama 1997; Inutsuka & Tsuribe 2001; Fiege & Pudritz 2000) and observationally (e.g., André et al. 2010; Arzoumanian et al. 2011, 2013; Kirk et al. 2013). A proposed scenario, especially supported by the results of the HGBS, is that large-scale turbulence, rather than large-scale gravity, plays the dominant role in forming interstellar filaments. However, gravity would appear to be the major driver in the subsequent evolution of the filaments, which may contract and accrete material from the background cloud, thus causing filaments to fragment into clumps and form (proto)stars under certain physical conditions.

Observationally, the gravitational fragmentation of filaments can be analyzed by comparing our Hi-GAL maps to existing models of filamentary cloud fragmentation. Inutsuka & Miyama (1997, and references therein) showed that an unmagnetized isothermal filament is unstable to axisymmetric perturbations if the line mass or mass per unit length, $M_{\rm line}$, of the filament is larger than the critical value required for equilibrium, $M^{\rm unmag}_{\rm line,crit} = 2\,c_{\rm s}^2/G$, where G is the gravitational constant. As shown by Ostriker (1964), the critical line mass depends on gas temperature only and, following Kirk et al. (2013), $M^{\rm unmag}_{\rm line,crit}$ can also be written in more convenient units as:

$$M^{\rm unmag}_{\rm line,crit} = 16.7 \left(\frac{T}{10\,{\rm K}}\right)\, M_\odot\,{\rm pc}^{-1}, \tag{18}$$

therefore if T is in the range of ≃10 to 15 K, then $M^{\rm unmag}_{\rm line,crit}$ is between ≃17 and 25 $M_\odot\,{\rm pc}^{-1}$. To derive the filament masses per unit length from our Hi-GAL maps, we used the radial column density profiles discussed in Sect. 5.1. The observed mass per unit length, $M_{\rm line}$, of the main and secondary filaments was then derived by integrating the measured average column density profile (as shown in Fig. 11) over radius, i.e., $M_{\rm line} = \mu_{\rm H_2}\, m_{\rm H} \int \langle N_{\rm H_2}(r)\rangle\, {\rm d}r$, where $\mu_{\rm H_2} = 2.8$ is the molecular weight per hydrogen molecule (Kauffmann et al. 2008) and $m_{\rm H}$ is the H-atom mass.

Because it is difficult to exactly define the edges of a filament, we decided to limit the range of integration to the 50% level of the peak value. If we use the 250 μm radial column density profile we obtain $M_{\rm line} \simeq 230$ and ≃50 $M_\odot\,{\rm pc}^{-1}$ for the main and secondary filaments[7], respectively. Both filaments would then appear to be supercritical, that is, gravitationally unstable with $M_{\rm line} > M^{\rm unmag}_{\rm line,crit}$. As a comparison, the values of $M_{\rm line}$ found in the literature vary in a wide range, from a few $M_\odot\,{\rm pc}^{-1}$ (e.g., Arzoumanian et al. 2013; Juvela et al. 2012b; Schisano et al. 2014) to as much as several 100s of $M_\odot\,{\rm pc}^{-1}$ (e.g., Contreras et al. 2013; Li et al. 2016; Schisano et al. 2014).

We note that while the main filament is highly supercritical, with $M_{\rm line}$ roughly ten times larger than the critical value, the secondary filament has a much lower $M_{\rm line}$ value. The total amount of support available in the main filament is therefore likely insufficient to keep the filament in equilibrium, implying that it should be radially contracting. This scenario assumes that unstable filaments would accrete additional mass from their surroundings and increase in mass per unit length while contracting with time. At the same time as they contract and accrete material from the background cloud, supercritical filaments are expected to fragment into clumps and form (proto)stars, giving rise to the morphology of the main filament and clumps shown in Fig. 1. However, as we noted in Sect. 4.2.2, we find no observational evidence showing that the gas is globally and radially infalling in either filament. This is either due to observational effects, related to the spectral lines used, or the radially contracting phase has already slowed down or stopped (or possibly not started yet, in the case of the secondary filament), thus being effectively undetectable.

Another alternative to explain the non-detection of radial infall toward the main filament is that all of the non-thermal motion is contributing thermal-like support. In this case one must consider the virial mass per unit length, $M_{\rm line,vir} = 2\,\sigma^2_{\rm av}/G$ (Fiege & Pudritz 2000), where $\sigma_{\rm av}$ is the velocity dispersion of the molecule of mean mass (see Sect. 4.3.2):

$$\sigma_{\rm av} = \frac{\Delta V_{\rm av}}{\sqrt{8\ln 2}}. \tag{19}$$

We note that $M_{\rm line,vir}$ is analogous to the virial mass and thus the dividing value between gravitationally unbound and bound filaments is defined by $M_{\rm line,vir} = 2\,M_{\rm line}$. Figures 7 and 8 can be used to estimate a typical velocity dispersion for the main filament, $\sigma_{\rm av} \sim 0.6\,{\rm km\,s^{-1}}$, and the secondary filament, $\sigma_{\rm av} \sim 0.4\,{\rm km\,s^{-1}}$. Thus we estimate $M_{\rm line,vir} \sim 70$ and ∼160 $M_\odot\,{\rm pc}^{-1}$ for the main and secondary filaments, respectively. Therefore, the thermally supercritical main filament is found to be a self-gravitating structure. The dynamical state of the secondary filament is instead much less defined, due to the uncertainty in the actual value used for $\sigma_{\rm av}$, and is thus at the edge of being in virial equilibrium or gravitationally unbound.

5.3. A possible evolutionary scenario

The noticeable separation between the (less evolved, younger; see Fig. 3) starless clumps and the (more evolved, older) protostellar clumps on the secondary and main filament, respectively, and the fact that the more massive and highly fragmented main filament is thermally supercritical and gravitationally bound, suggest a later stage of evolution of the main filament. In the main filament clumps have accreted enough mass to become mostly protostellar, and the molecular gas surrounding them appears to be more turbulent compared to starless clumps, as shown in Sect. 4.2.2. Also, the more diffuse gas in the main filament shows a higher degree of turbulence compared to the secondary filament. A trend of increasing $\sigma_{\rm av}$ with $M_{\rm line}$ has in fact been discussed by Arzoumanian et al. (2013).

[7] No projection effects have been considered.

As mentioned in Sect. 4.2.1 we observe a velocity gradient along the main axis of the filament, and we have discussed several possible interpretations for this gradient. It is however interesting to discuss in greater details the explanation of this velocity gradient in terms of a possible accretion flow from the filament onto the central cluster. A similar scenario has indeed been proposed for the case of the Serpens South filament and cluster, though with a higher value of dV/dr (Kirk et al. 2013). A difficulty with this interpretation is that in our main filament the protostellar clumps are actually distributed along the entire length of the structure (see Figs. 1 and 6), though there is a main cluster of clumps in the NW section of the filament.

The much less massive secondary filament, which is also marginally supercritical, appears to have a smoother and regular profile (as confirmed by the narrow shaded area, indicating the standard deviation, in Fig. 11). As we mentioned already it contains only starless clumps, and the less turbulent ambient gas and its dynamical state (gravitationally unbound or near to virial equilibrium) suggest that this structure could be in an earlier evolutionary phase. Alternatively, this low-density filament may have evolved differently from the main filament, and its current dynamical state may prevent any further accretion. However, our spectral line maps are not extended enough to determine whether molecular gas is actually flowing from the ambient gas also toward the secondary filament, and whether it could eventually follow the same evolutionary path of its main counterpart.

If this low-density filament is indeed unbound it may be expected to disperse on a turbulent crossing time, unless it is confined by some external pressure. Arzoumanian et al. (2013) also suggest that low-density filaments, observed roughly perpendicular to the main supercritical filaments, could be feeding them contributing to their accretion process and growth in mass per unit length. The velocity gradient measured along the secondary filament and shown in Fig. 6 is roughly directed toward the main filament, and appears to point toward the bright region located at the center-south (RA $\sim 07^{\rm h}10^{\rm m}$, Dec $\sim -10°30'$) of both Hi-GAL and spectral line maps (see Figs. 1, 2 and 5), which also corresponds to a higher concentration of protostellar clumps. However, as noted in Sect. 4.2.1, this velocity gradient is less reliable compared to that measured along the main filament.

Therefore, if we use the simple method discussed by Kirk et al. (2013) to estimate the mass accretion rate implied by the velocity gradient along the main filament, we obtain an accretion rate along the filament onto the two main clusters of protostellar clumps of $\sim$100 $M_\odot$/Myr, assuming the inclination of the filament to the plane of the sky is exactly 0, and also assuming that the observed velocity gradient has not an entirely different kinematical origin (e.g., rotation). We can compare this estimate of the accretion rate with the star-formation rate (SFR), $\simeq$260 $M_\odot$/Myr, found by Elia et al. (2013) for the $\ell = 224°$ region. Thus we can see that our estimate of the mass accretion rate is comparable with the mass supply required to form the current generation of YSOs along the main filament. This result suggests that filamentary accretion may significantly affect the formation and evolution of stars along the main filament.

6. Conclusions

Using the Hi-GAL dust continuum information and analyzing the Mopra spectral line maps, we study the distribution of starless and protostellar clumps as well as the dynamics of the two filaments observed toward the $\ell = 224°$ region. The protostellar clumps are more luminous and more turbulent compared to the starless clumps, and also lie in regions where the filamentary ambient gas shows larger linewidths. The more massive and highly fragmented main filament appears to be thermally supercritical and gravitationally bound, suggesting a later stage of evolution compared to the secondary filament, which is gravitationally unbound (or near to virial equilibrium) and hosts less turbulent ambient gas. Therefore, the low-density secondary filament is either in an earlier evolutionary phase, or it may have evolved differently from the main filament, and its current dynamical state may prevent any further accretion. The status and evolutionary phase of the Hi-GAL clumps would then appear to correlate with that of the host filament.

Our observations show a velocity gradient along the main filament. If this gradient is indeed associated with a mass flow along the filament, possibly feeding the main two clusters of protostellar objects, then the estimated mass accretion rate would be high enough to lead to the formation of several tens of YSOs (of mean mass 0.5 $M_\odot$) in a few Myr. Our observations also indicate that there might be gas flow from the secondary filament onto the two main clusters of protostellar clumps located on the main filament. To assess the reliability of this tentative scenario as well as to investigate the presence of infalling gas from the filament onto the clusters, the area covered by our Mopra maps would need to be extended and different spectral lines, such as HCO^+ and $H^{13}CO^+$ (1–0), should be used.

Acknowledgements. The Mopra radio telescope is part of the Australia Telescope National Facility which is funded by the Australian Government for operation as a National Facility managed by CSIRO. The University of New South Wales Digital Filter Bank used for the observations with the Mopra Telescope was provided with support from the Australian Research Council. The authors wish to thank the staff of the Mopra Observatory for the support provided before and during the observations. D.E.'s research activity is supported by the European Union Seventh Framework Programme (FP7/2007-2013) under grant agreement No. 607380 (VIALACTEA: the Milky Way as a star-formation engine).

References

André, P., Men'shchikov, A., Bontemps, S., et al. 2010, A&A, 518, L102
André, P., Revéret, V., Könyves, V., et al. 2016, A&A, 592, A54
Arzoumanian, D., André, P., Didelon, P., et al. 2011, A&A, 529, L6
Arzoumanian, D., André, P., Peretto, N., & Könyves, V. 2013, A&A, 553, A119
Contreras, Y., Rathborne, J., & Garay, G. 2013, MNRAS, 433, 251
Curtis, E. I., & Richer, J. S. 2011, MNRAS, 410, 75
De Vries, C. H., & Myers, P. C. 2005, ApJ, 620, 800
Elia, D., Schisano, E., Molinari, S., et al. 2010, A&A, 518, L97
Elia, D., Molinari, S., Fukui, Y., et al. 2013, ApJ, 772, 45
Fiege, J. D., & Pudritz, R. E. 2000, MNRAS, 311, 85
Fontani, F., Cesaroni, R., Caselli, P., & Olmi, L. 2002, A&A, 389, 603
Frerking, M. A., Langer, W. D., & Wilson, R. W. 1982, ApJ, 262, 590
Goodman, A. A., Benson, P. J., Fuller, G. A., & Myers, P. C. 1993, ApJ, 406, 528
Hacar, A., Tafalla, M., Kauffmann, J., & Kovács, A. 2013, A&A, 554, A55
Indermuehle, B., Edwards, P., Brooks, K., & Urquhart, J. 2013, in CSIRO Data Archive, DOI: 10.4225/08/521A8EF38E042
Inutsuka, S.-I., & Miyama, S. M. 1997, ApJ, 480, 681
Inutsuka, S.-I., & Tsuribe, T. 2001, in The Formation of Binary Stars, eds. H. Zinnecker, & R. Mathieu, IAU Symp., 200, 391
Juvela, M., Malinen, J., & Lunttila, T. 2012a, A&A, 544, A141
Juvela, M., Ristorcelli, I., Pagani, L., et al. 2012b, A&A, 541, A12
Kauffmann, J., Bertoldi, F., Bourke, T. L., Evans, II, N. J., & Lee, C. W. 2008, A&A, 487, 993

Kim, B. G., Kawamura, A., Yonekura, Y., & Fukui, Y. 2004, PASJ, 56, 313
Kirk, H., Myers, P. C., Bourke, T. L., et al. 2013, ApJ, 766, 115
Ladd, N., Purcell, C., Wong, T., & Robertson, S. 2005, PASA, 22, 62
Li, G.-X., Urquhart, J. S., Leurini, S., et al. 2016, A&A, 591, A5
Lis, D. C., & Goldsmith, P. F. 1991, ApJ, 369, 157
MacLaren, I., Richardson, K. M., & Wolfendale, A. W. 1988, ApJ, 333, 821
Markwardt, C. B. 2009, in Astronomical Data Analysis Software and Systems XVIII, eds. D. A. Bohlender, D. Durand, & P. Dowler, ASP Conf. Ser., 411, 251
Martin, P. G., Roy, A., Bontemps, S., et al. 2012, ApJ, 751, 28
Molinari, S., Pezzuto, S., Cesaroni, R., et al. 2008, A&A, 481, 345
Molinari, S., Swinyard, B., Bally, J., et al. 2010, PASP, 122, 314
Nutter, D., Kirk, J. M., Stamatellos, D., & Ward-Thompson, D. 2008, MNRAS, 384, 755
Olmi, L., Anglés-Alcázar, D., Elia, D., et al. 2013, A&A, 551, A111
Ostriker, J. 1964, ApJ, 140, 1056
Polychroni, D., Schisano, E., Elia, D., et al. 2013, ApJ, 777, L33
Pon, A., Johnstone, D., & Heitsch, F. 2011, ApJ, 740, 88
Schisano, E., Rygl, K. L. J., Molinari, S., et al. 2014, ApJ, 791, 27
Schneider, N., Csengeri, T., Bontemps, S., et al. 2010, A&A, 520, A49
Wilson, T. L., & Rood, R. 1994, ARA&A, 32, 191
Wilson, T. L., Serabyn, E., Henkel, C., & Walmsley, C. M. 1986, A&A, 158, L1

Appendix A: Channel maps

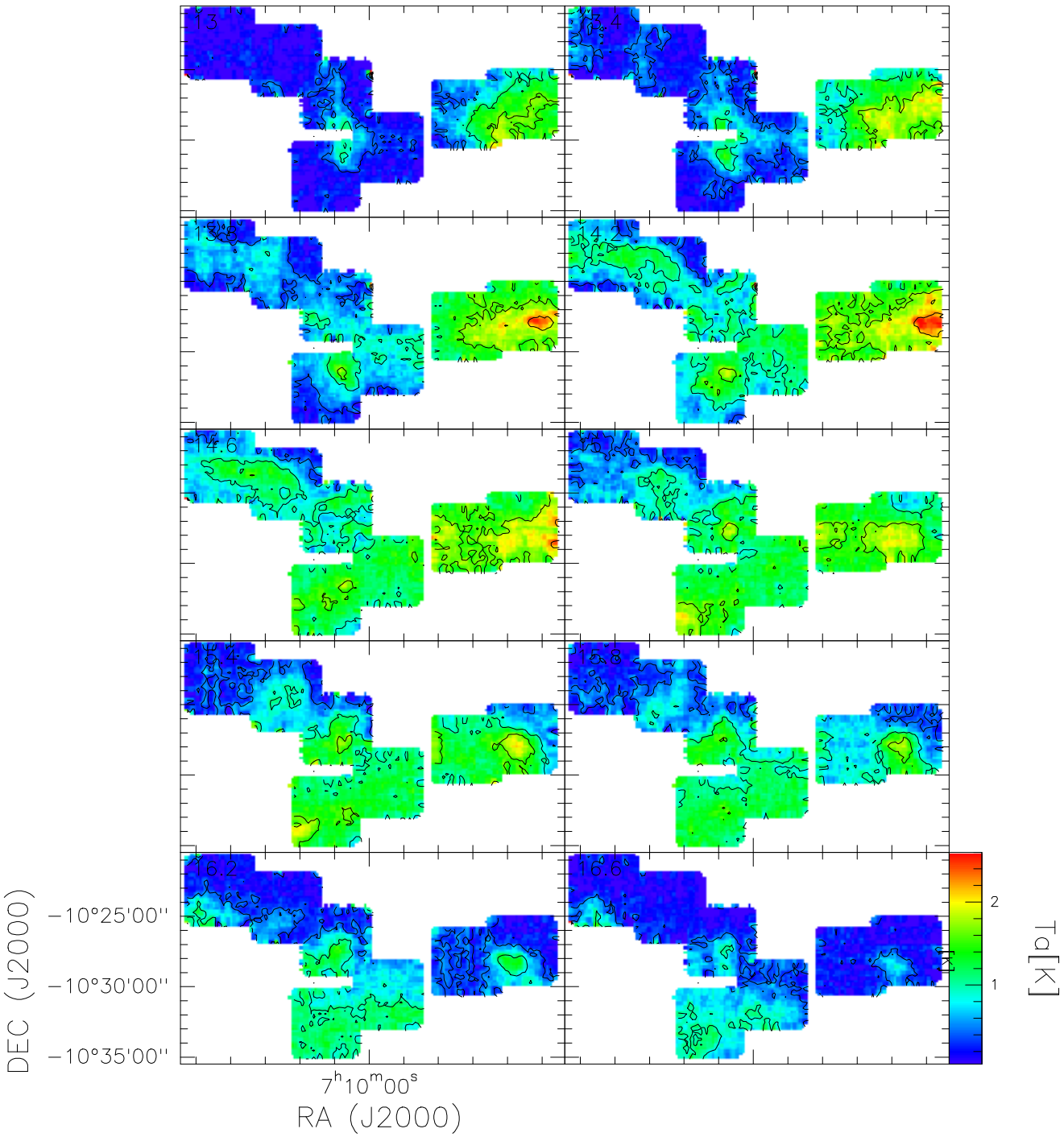

Fig. A.1. Channel maps of ^{13}CO(1−0), between 13 and 16.6 km s^{-1} (as shown in the top-left corner of each panel). The isolated individual region, centered at (RA, Dec) ~ (07:11:18, −10:36:00), has been dropped from this figure to increase visibility of the main regions of emission.

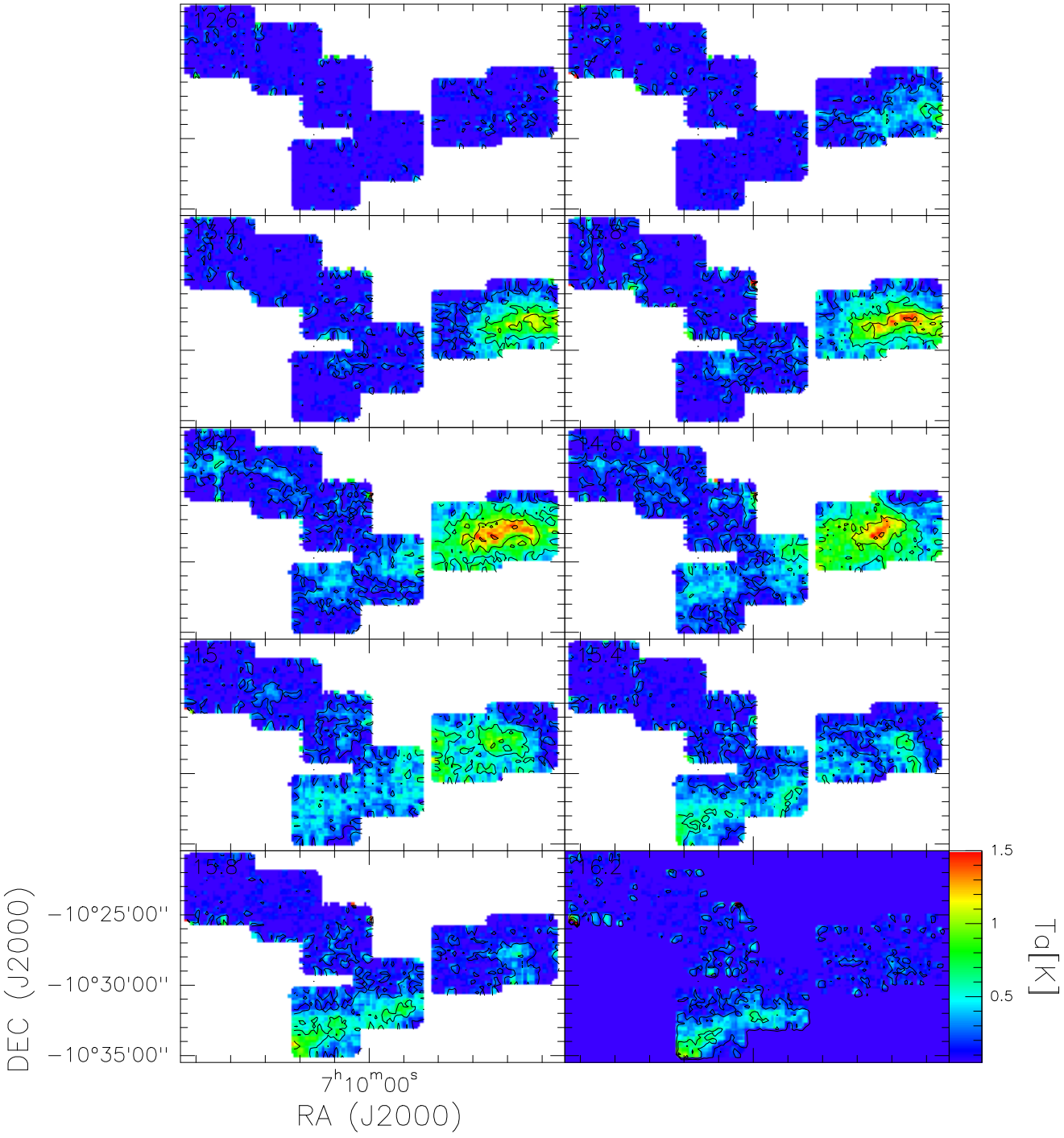

Fig. A.2. Same as Fig. A.1 for $C^{18}O(1-0)$.

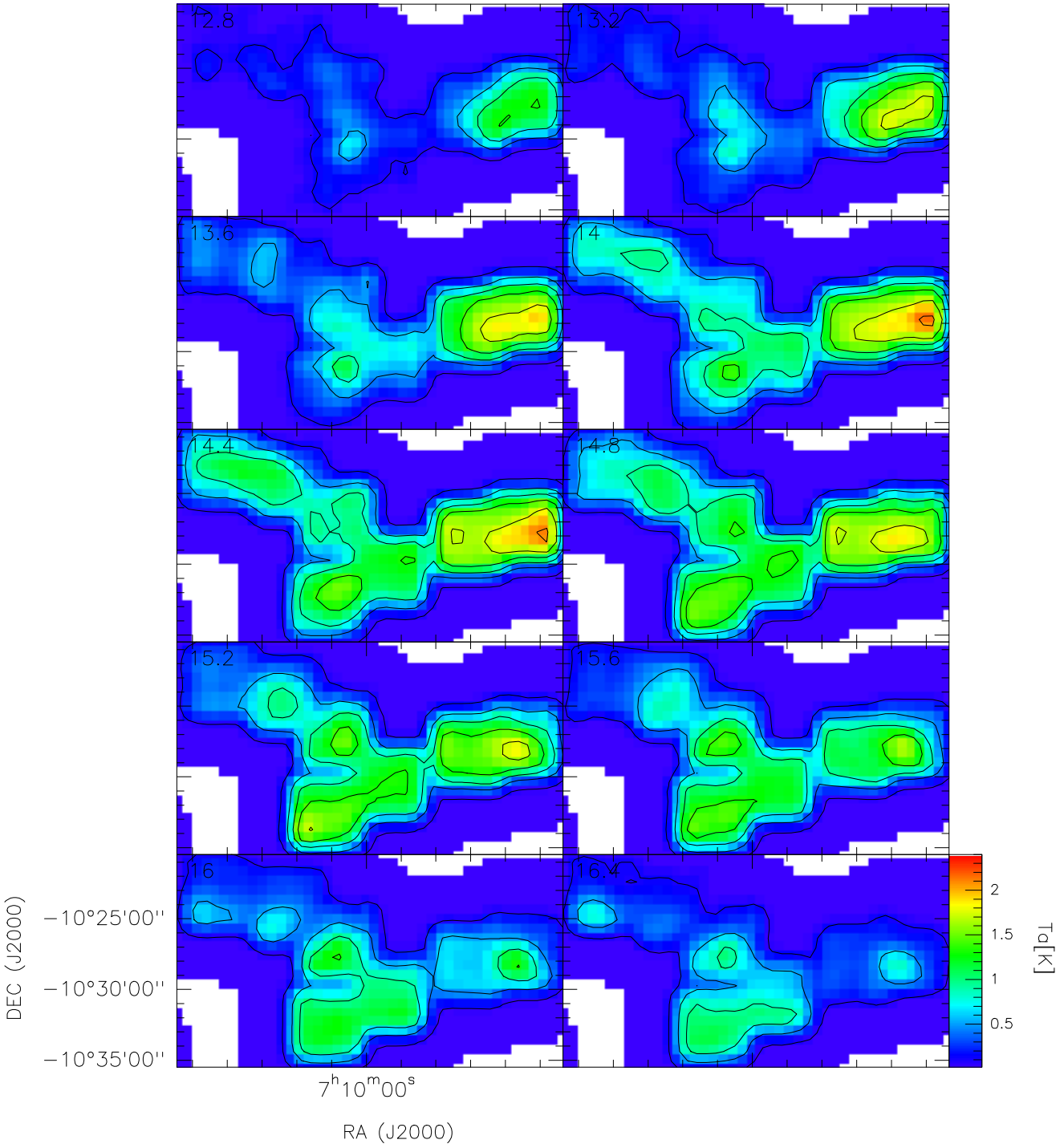

Fig. A.3. Same as Fig. A.1, after convolving the map with a 80 arcsec beam and re-gridding the map on a 40 arcsec step.

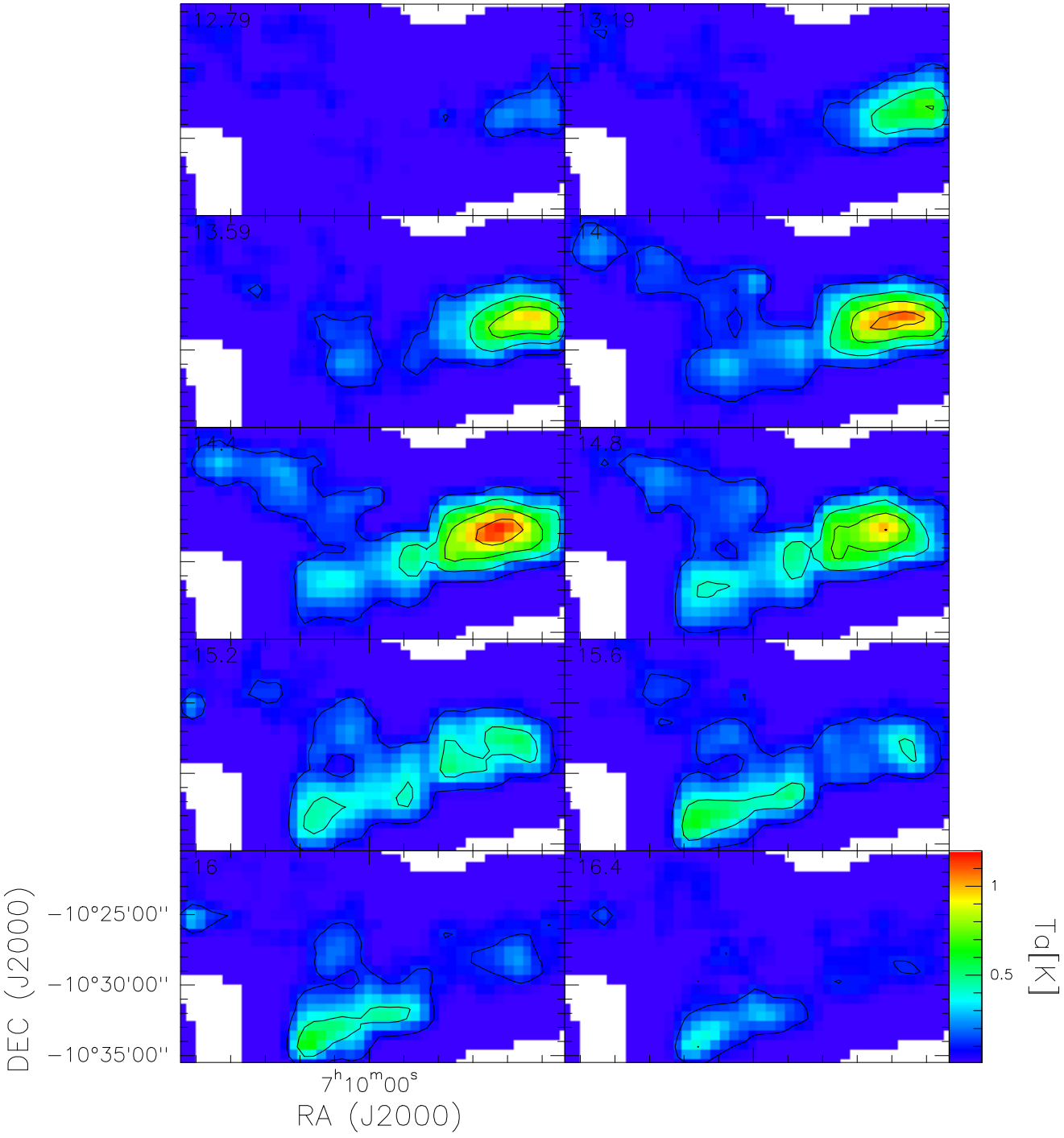

Fig. A.4. Same as Fig. A.3 for $C^{18}O(1-0)$.

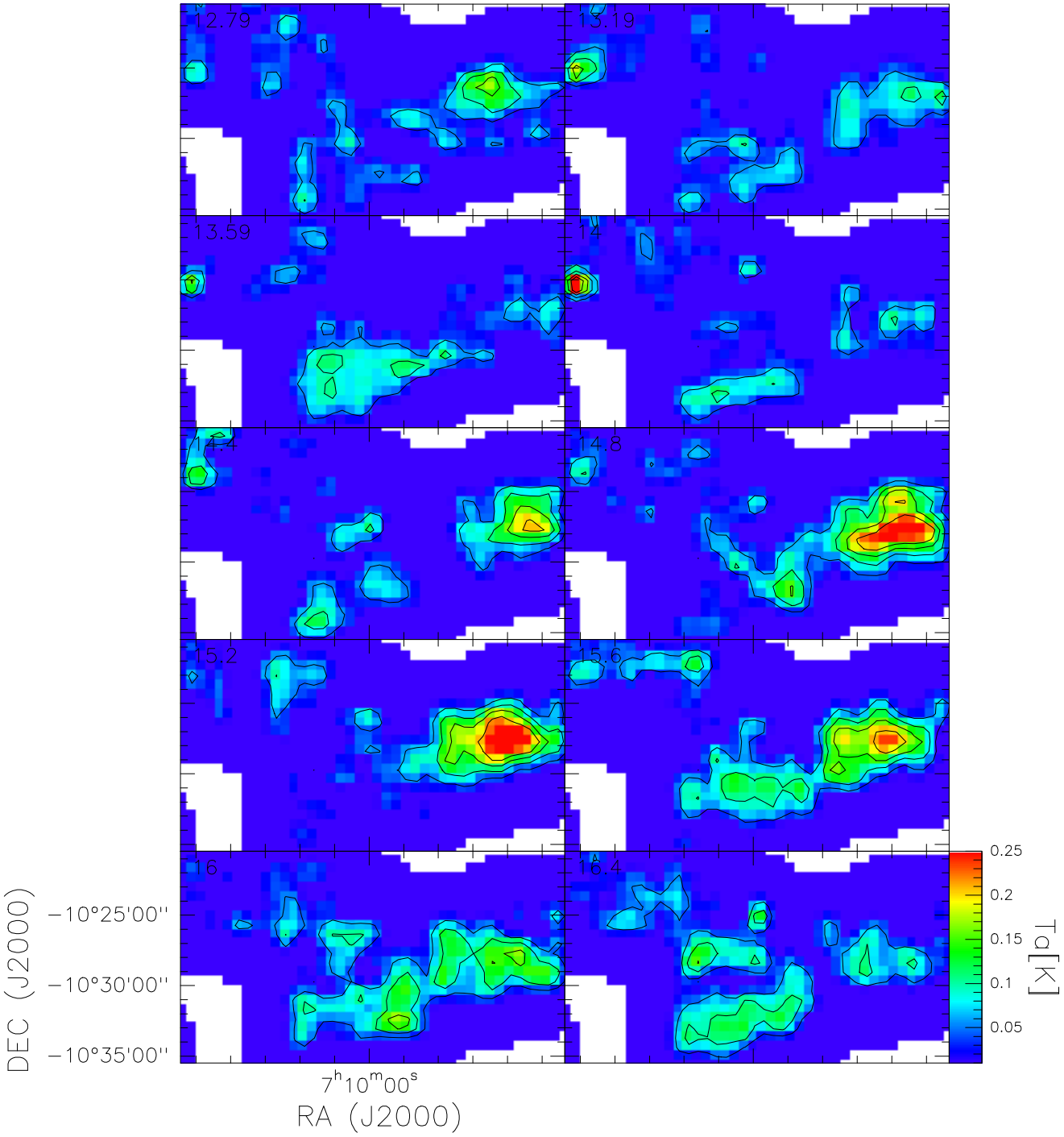

Fig. A.5. Same as Fig. A.3 for $C^{17}O(1-0)$.